OBSERVATIONS AND PARAMETERIZATIONS OF PARTICLE SIZE DISTRIBUTIONS IN DEEP TROPICAL CIRRUS AND STRATIFORM PRECIPITATING CLOUDS: RESULTS FROM IN—SITU OBSERVATIONS IN TRMM FIELD CAMPAIGNS

Andrew J. Heymsfield and Aaron Bansemer
National Center for Atmospheric Research
Boulder, Colo.

Paul R. Field
Met. Res. Flt., U.K. Met Office
Farnborough, U.K.

Stephen L. Durden
Jet Propulsion Laboratory
Pasadena, Calif.

Jeffrey L. Stith, James E. Dye, and William Hall
National Center for Atmospheric Research
Boulder, Colo.

Cedric A. Grainger
University of North Dakota
Grand Forks, N.D.

* Manuscript Accepted: *May* 2002

Corresponding author address: Andrew Heymsfield
3450 Mitchell Lane
Boulder, Colorado 80301
heyms1@ncar.ucar.edu

ABSTRACT

In this study, we report on the evolution of particle size distributions (PSDs) and habits as measured during slow, Lagrangian-type spiral descents through deep subtropical and tropical cloud layers in Florida, Brazil, and Kwajalein, Marshall Islands, most of which were precipitating. The objective of the flight patterns was to learn more about how the PSDs evolved in the vertical and to obtain information of the vertical structure of microphysical properties. New instrumentation yielding better information on the concentrations of particles in the size (D) range between 0.2 and 2 cm, as well as improved particle imagery, produced more comprehensive observations for tropical stratiform precipitation regions and anvils than have been available previously. Collocated radar observations provided additional information on the vertical structure of the cloud layers sampled.

Most of the spirals began at cloud top, with temperatures (T) as low as —50°C, and ended at cloud base or below the melting layer (ML). The PSDs broadened from cloud top towards cloud base, with the largest particles increasing in size from several millimeters at cloud top to one centimeter or larger towards cloud base. Some continued growth was noted in the upper part of the ML. Concentrations of particles less than 1 mm in size decreased with decreasing height. The result was a consistent change in the PSDs in the vertical. Similarly, systematic changes in the size dependence of the particle cross-sectional area was noted with decreasing height. Aggregation—as ascertained from both the changes in the PSDs and evolution of particle habits as observed in high detail with the cloud particle imager (CPI) probe—was responsible for these trends.

The PSDs were generally well-represented by gamma distributions of the form $N = N_{0\Gamma} D^{\mu} e^{-\lambda_{\Gamma} D}$ that were fitted to the PSDs over 1—km horizontal intervals throughout the spirals. The intercept ($N_{0\Gamma}$), slope (λ_{Γ}), and dispersion (μ) values were derived for each PSD. Exponential curves ($N = N_0 e^{-\lambda D}$; $\mu = 0$) were also fitted to the distributions. The λ_{Γ} values for given spirals varied systematically with temperature as did the values of λ (exponential), and the data generally conformed to values found in previous studies involving exponential fits to size distributions in mid-latitude frontal and cirrus layers. Considerable variability often noted in the PSD properties during the loops of individual spirals was manifested primarily in large changes in $N_{0\Gamma}$ and N_0, but μ, λ_{Γ} and λ remained fairly stable. Temperature is not found to be the sole factor controlling λ_{Γ} or λ but is a primary one. Direct relationships were found between λ_{Γ} and $N_{0\Gamma}$ or λ_{Γ} and μ for the gamma distributions and λ and N_0 for the exponential. The latter relationship was not found as distinctly in earlier studies; observed PSDs in this study had better fidelity with less scatter. The μ values changed monotonically with T over the range of temperatures and were directly related to $N_{0\Gamma}$ or λ_{Γ} , thereby reducing the number of variables in the PSD functional equation to two. In the upper part of the ML, N_0 and λ continued to decrease, and in the lower part these values began to increase as the largest particles melted.

We developed general expressions relating various bulk microphysical, radar, and radiative transfer—related variables to $N_{0\Gamma}$ and λ_{Γ} , useful for both tropical and mid-latitude clouds. These relationships facilitate the specification of a number of bulk properties in cloud and climate models. The results presented in this paper apply best to temperatures between 0 and —40°C, for which the measured radar reflectivities fall in the range of 0 to 25 dBZ_e.

1.INTRODUCTION

During 1998 and 1999, four field campaigns were conducted by the Tropical Rainfall Measuring Mission (TRMM) to evaluate the performance of the TRMM radar and radiometer retrieval algorithms. These field programs also provided validation data for TRMM mesoscale and regional—scale models. The experiments were conducted in subtropical and tropical regions: Texas and Florida (TExas-FLorida UNderflights, TEFLUN-A and B), Brazil (Large Scale Biosphere-Atmosphere Experiment, LBA) and Kwajalein, Marshall Islands (Kwajalein Experiment, KWAJEX). Measurements were acquired using multipolarization ground-based Doppler radars, rain gauges, and in—situ and overflying aircraft. As part of the validation effort, in TEFLUN-B, LBA, and KWAJEX, the University of North Dakota (UND) Citation aircraft employed state—of—the–art instrumentation to acquire in—situ measurements. In this study, we report on microphysical data acquired by the Citation in deep tropical anvils and stratiform precipitating clouds and develop parameterizations for use by the remote—sensing and modeling communities.

Past in—situ microphysical observations in tropical ice clouds over the range —80 $\leq$ T $\leq$ -20°C have provided indications of total particle concentrations (N_t) and ice water contents (IWC). In the primary studies, listed in Table 1, particles with minimum diameter of between 10 and 100 μm up to about 1 mm were measured. Griffith *et al.* (1980) found that the IWCs in three cirrus cloud decks sampled at multiple levels during the GARP Atlantic Tropical Experiment (GATE) generally increased from near cloud top (11.5 to 13.0 km) to near cloud base (7 to 9.5 km); peak, level-averaged IWCs reached 0.05 g m^{-3}. Knollenberg *et al.* (1982, 1993) reported IWCs as high as several hundredths g m^{-3} in anvil cirrus near Panama and in cirrus at the top of a cyclone off the northwest coast of Australia, both at $T \approx$ —80°C. Takahashi and Kuhara (1993) used videosondes to characterize the properties of cumulonimbus clouds over Pohnpei, Micronesia at T values as low as -80°C. They found that peak IWC and maximum diameter decreased with height (T) and approached the amounts reported by Griffith *et al.* (1980) and Knollenberg *et al.* (1982) at lower values for T. Pueschel *et al.* (1995) reported on ice particle measurements in a typhoon over the range —40 $\leq T \leq$ 0°C. The highest concentrations and smallest particles were observed near -40°C. The microphysical characteristics of convectively generated ice clouds over the range —70 to —20°C, from observations near Kwajalein, and during the Central Equatorial Pacific Experiment (CEPEX), were described in Heymsfield and McFarquhar (1996) and McFarquhar and Heymsfield (1996). Average IWCs over this range of T increased from about five thousandths to several tenths gram m^{-3}, and IWC, cross-sectional area, and median mass-weighted diameter increased downward below cloud top.

Stith et al. (2002), from the TRMM field campaigns described below, showed that there was a wide variety of particle types observed both in the convective and stratiform regions of tropical ice clouds at temperatures from 0 to about -20°C, using data primarily from the cloud particle imager and 2D-C probes. Aggregation was observed to be a primary growth process, as was also the case in the Heymsfield and McFarquhar (1996) study.

Although remote—sensing and modeling applications require knowledge of the PSDs in tropical clouds, relatively little data have been available to develop parameterizations for these PSDs. The PSDs of cirrus anvils and detached cirrus sampled during CEPEX were characterized by McFarquhar and Heymsfield (1997). They parameterized concentration in terms of the melted equivalent diameter (D_m) as a function of IWC and T. A limitation of the data set was that concentrations of particles with size above approximately 0.1 cm were generally below the detection limit of the 2D-C probe.

This discussion of previous studies implies important gaps in our knowledge of tropical ice cloud microphysical properties. In particular, few observations have been made of PSDs for particle sizes above 0.1 to 0.2 cm, or for T in the range 0 to —20°C. There are also few observations of how PSDs vary in the vertical—other than those made by combining horizontal flight legs at different altitudes—or of microphysical properties as related to radar echoes. Furthermore, little information is available on particle habits. The data in this study fill some of these gaps. Spiral descents were used to characterize microphysical properties in the vertical for temperatures in the range —50 to 0°C. Recently developed probes that provide high-quality particle habit information, especially for the smaller particle sizes, were used. Also, considerably larger sampling volumes in the larger sizes provided more reliable measurements of PSDs than those previously obtained for tropical ice clouds.

In section 2, we describe new instrumentation used for this study. We present our observations in section 3. IWCs and other bulk properties derived from the PSDs are given in section 4; we also develop parameterizations to represent these properties. In section 5, we compare our results to earlier observations in mid-latitude and tropical ice clouds. We conclude in section 6 by summarizing the results of this study. A list of symbols used for the different cloud microphysics variables is given in Appendix A, and the methods used to calculate particle mass and terminal velocity are given in Appendix B.

2.INSTRUMENTATION AND DATA PROCESSING

The microphysical data sets collected during the TRMM field campaigns probably constitute the most complete set of in—situ data in subtropical and tropical clouds to date.

On the UND Citation aircraft, particle shapes were imaged and size distributions measured from about 20 μm to >2 cm.

A Stratton Park Engineering Co.(SPEC), Inc., cloud particle imager (CPI) probe provided detailed information on the shapes and sizes of particles from approximately 20 μm to above 1 mm, with 2.3 μm resolution. Because the CPI sampling volume is relatively small and is still the subject of study, the size distributions obtained from the CPI are not used here.

PSDs, along with low—resolution particle imagery, were obtained from the Particle Measuring Systems (PMS) 2D-C and the SPEC high volume particle spectrometer (HVPS) probes. The PSDs were measured from 33 μm to above 1 mm in 33 μm increments by the 2D-C, and from 0.2 mm to about 5 cm in increments of 0.2 mm from the HVPS, with composite PSDs generated from the two probes by finding a point at which the size distributions from each overlapped, or where the concentrations were comparable. The overlap size usually occurred from 1 to 2 mm. The nominal 2D-C probe sample volume is given by the probe's array width (about 1 mm) times the separation between the probe's arms (6.1 cm) times the Citation's true airspeed (about 120 m s^{-1}), or about 7 l s^{-1}. The "particle reconstruction" technique was used to extend this sample volume by an amount that increased roughly linearly with size (see sample volume values in Heymsfield and Parrish, 1979), by considering particles that were partially outside of the 2D-C probes' sample volume. The HVPS swept out a sample volume given by the array width (about 5 cm) times the separation between the probes' arms of about 20 cm, times the aircraft's true airspeed, or about 1 m^{-3} s^{-1}.

In general, the 2D-C probe worked well during the various TRMM field campaigns, although concentrations between 33 and 100 μm are generally considered to be inaccurate because of questions related to the probe's sample volume in this size range. The HVPS worked poorly in the TEFLUN experiments, worked intermittently in LBA, and worked well in KWAJEX. Therefore, examination of the vertical variability of the PSD emphasizes the KWAJEX spirals. Useful CPI imagery was obtained from the spirals in all field programs.

Key imaging probe data required for our analysis included the maximum particle diameter (D), cross-sectional area (A), area ratio ($A_r = \frac{A}{\frac{\pi}{4}D^2}$), and concentration per size bin (N_i). The diameter was derived as the "true" maximum diameter—not the maximum diameter along the array or flight direction axes, as in previous calculations.

State parameters were obtained from the aircraft's standard suite of instruments. The T measurement, from a heated Rosemount sensor, is accurate to approximately $\pm$ 0.5°C.

A more complete discussion of the Citation state parameter instrumentation appears in Stith et al. (2002).

We used Doppler radar data from the ER-2 and DC-8 aircraft to characterize the reflectivity structure of the cloud layers during the Citation sampling, and ground-based S band (10.7 cm) radar data to examine temporal evolution of the cloud layers during the spirals. The ER-2 Doppler radar (EDOP) transmits at a wavelength of 3.1 cm (G. Heymsfield, 1996), whereas the airborne mapping Doppler radar (ARMAR) on the DC-8 transmits at a wavelength of 2.2 cm (Durden et al., 1994). The vertical resolution of these radars is 80 m (ARMAR) and 75 m (EDOP); the minimum detectable reflectivity as used here is approximately —10 dBZ_e; and the precision of the velocity estimate (particle fall velocity + air velocity) is 0.1 m s^{-1}. The vertical motions of each aircraft have been subtracted from the velocity estimates by using the Doppler velocity information in the lowest (surface) rangegate, together with the aircraft navigational system data to remove the aircraft vertical motion. Some random components of vertical motion could not be subtracted but were eliminated through averaging [1], which resulted in an absolute accuracy of the Doppler velocities of $\pm$ 0.3 m s^{-1} for the ARMAR radar but was 0.5–1.0 m s^{-1} for EDOP. The accuracy of the reflectivity measurements from each aircraft radar was approximately $\pm$ 1 dB. No aircraft Doppler data were available for three of the flights examined later but data from the ground-based radar for these flights was available. The ground-based radars included the NCAR S-pol radar during TEFLUN-B and LBA and a similar S-band radar during KWAJEX. (The characteristics of the KWAJEX radar are presented in Schumacher and Houze, 2001).

3. OBSERVATIONS

A. Sampling Strategy and Limitations

The data reported here were collected primarily in anvils and dissipating thick stratiform precipitation regions. As pointed out by Field (1999), "it is quite common for an aircraft run at a given height to encounter a cloud that thins, breaks, and perhaps thickens again. If microphysical data are averaged over such a traverse it becomes difficult to disentangle the effects of differing local conditions on the evolution of the particle population". It is therefore difficult to assess how the properties of a cloud change in the vertical from data averaged for different levels.

To examine vertical variability but particularly particle evolution in the vertical, each case studied here involved a Lo and Passarelli (1982) type Lagrangian spiral descent through

[1] Possible upward motions in and above the vicinity of the radar bright band of order ten cm s^{-1} would not have been eliminated by averaging but will not significantly influence the results.

a cloud to observe the evolution of the PSDs. A vertical profile using this technique starts aloft in a horizontally extensive ice cloud area, and an aircraft is placed in a constant bank angle at a constant descent rate of about 1 m s^{-1}. The aircraft spirals downward at approximately the mean fallspeed of the snow and the loops of the spiral drift with the wind. Ideally, if conditions are quasi-steady and the properties of the atmosphere are fairly uniform over a length scale somewhat larger than the diameter of the loops, then the aircraft largely samples particle evolution from the height change in the size distribution properties. The analysis of particle size spectra can be performed by averaging spectra over a complete loop of the spiral. This serves to average any horizontal inhomogeneities. Another approach is to compare particle size spectra at various heights that occurred in the same aircraft heading or sector of different loops. Ideally, if all the loops are the same size and the aircraft descends at about 1 m s^{-1}, then each point of the aircraft trajectory corresponds to the trajectory of a 1 m s^{-1} particle.

Horizontal gradients in wind velocity, wind shear and dispersion of ice particle fallspeed creates a difficult sampling problem under the best of circumstances. For example, even if the cloud dynamics and microphysics are in a quasi-steady state, there are usually mesoscale areas of precipitation embedded within widespread cloud layers which move and change with time. Our observations are much more prone to sampling errors and misinterpretation than earlier studies that used Lagrangian spiral descents to sample stratiform cloud layers. This is in part because temporal evolution was much more pronounced—the durations of the spirals were comparable to the life cycles of the convective clouds that generated the cloud layers, such that the upper portions of the cloud we sampled could have evolved substantially by the time we sampled the lower portions of the clouds. Furthermore, horizontal inhomogeneities are possibly more pronounced than in widespread cloud layers–small convective elements could have contributed concentrated but small-scale regions embedded within broader cloud layers.

The vertical variations in the PSD properties that are presented in this section therefore may not represent the properties at any given time. What is being observed is the changes downwards in the part of the PSD falling at the descent velocity of the aircraft, whether or not there is substantial evolution of the cloud properties above the sampling level. For each case studied, the extent of evolution of the radar echoes over the course of the descents will be characterized and the impact discussed in Section 5. Note also that horizontal variability in the properties of the PSDs during the course of each spiral may be more extensive than in earlier studies, a factor that will also be discussed in Sections 3C and 5. And lastly, the spiral descents occupied less than five hours of aircraft flight time whereas there is almost 100 hours of data collected during horizontal traverses. This broader set

of data will be used in the future to study the relationship between radar reflectivity and properties of the PSD for tropical ice clouds in forthcoming articles planned by a number of investigators.

B. Overview of the Cloud Layer Properties

The cloud top and base heights and temperatures measured by the aircraft during the spirals, the cloud optical depths estimated from the microphysical probes, and the changes in the radar reflectivities of the regions of the clouds sampled during the spirals are presented in Table 2. Most spirals commenced at cloud top, with four descents initiating at temperatures below —35°C and five above —20°C (Table 2). In the coldest case, $T =$ — 50°C. The spirals ended at cloud base, or in rain when the cloud base was below the ML, and spanned a cloud depth that was usually between 3.0 and 4.5 km. When possible, aircraft descent rates $\frac{d(Alt)}{dt}$ were adjusted to match the approximate mean particle fallspeeds both in the ice (1 to 2 m s^{-1}) and rain (5 to 7 m s^{-1}) regions. These attempts were successful in KWAJEX but not in LBA (Table 2, $\overline{\frac{d(Alt)}{dt}}$).

Each loop of the spiral spanned a diameter of 5 to 10 km, with the number of loops varying from 3 to 23, exceeding 10 for all KWAJEX cases. The Citation drifted several tens of kilometers with the wind during the sampling periods (Fig. 1), ranging from 6 to 45 minutes with most in the 25 to 45 minute range.

An average optical depth for each spiral descent was derived by integrating downwards from the top to the base of the spiral, twice the cross-sectional area of the particle population as measured by the 2D-C and HVPS probes (Table 2). The cloud layers sampled were close to or exceeded the value of 23 necessary to be considered within the "Deep Convection" cloud category according to the International Satellite Cloud Climatology Project (ISCCP, Rossow and Schiffer, 1999). Our clouds did not fall within the optically thinner categories of "Cirrus" or "Cirrostratus".

As shown in Table 2, "Radar" from the ground-based S-band radars, nine of the ten spiral descents were associated with precipitation (deduced from radar) at some time during the spirals. Most of the clouds would have had surface reflectivities above the 18 dBZ_e or so necessary to be detected by the TRMM radar. (TEFLUN-B data courtesy Ed Brandes, LBA data courtesy Walt Petersen, KWAJEX data courtesy Sandra Yuter).

Coincident vertical profiles of the measured radar reflectivities (dBZ_e) and reflectivity-weighted Doppler particle fallspeeds (V_Z, positive downward) were available from overflying aircraft during seven of the spirals. The measured V_Z values are the sum of the air and particle velocities. The ARMAR or EDOP provided information during or shortly before these spirals (Fig. 1). Note that the radar data were nearly instantaneous, although the Citation spirals required 30 minutes or so and involved aircraft drift. While a one-to-

one comparison of the radar and in-situ measurements is therefore not possible , pertinent information on cloud structure, measured dBZ$_e$, V_Z, and presence of significant updrafts were obtained, at least for some portion of the spirals. Periods were identified when the Citation and DC-8 or ER-2 tracks overlapped (bold lines, Fig. 1), and radar data during and near these periods were examined to assess the adjacent cloud structure.

Averaged vertical profiles of measured dBZ$_e$ and V_Z for various periods of aircraft coincidence are shown in Fig. 2, left and right panels. The dBZ$_e$ in the ice regions (4.5 km above mean sea level) fell in the 5 —25 dBZ$_e$ range and generally increased downwards. The trend differed for the 990819 case (top panels), in which the dBZ$_e$ values were nearly constant with height. The V_Z in ice were 1 to 2 m s^{-1}, also usually showing an increase downward. Vertical air motions may have been present in the data from individual radar scans, but averaging over the relatively long horizontal intervals probably canceled out up- and downdrafts, with the exception of possible local upward motions of order 10 cm s^{-1} at and above the melting layer. Vertical air motions also contributed to the $\pm$ 1σ bounds of 50 to 100 cm s^{-1} shown in the figure. Lower V_Z generally coincided with lower dBZ$_e$. Bright bands—e.g., melting layers—were noted in the data at approximately 4.5 km in five of the cases. Below 4.2 km in rain, the Z$_e$ values were 20 to 30 dBZ$_e$, except on 990911, when lower values for dBZ$_e$ were measured. The values for V_Z in rain were about 6 m s^{-1}.

To place some bounds on the extent of temporal evolution during the spirals, airborne and ground-based radar measurements were used to loosely examine the change in the mean radar reflectivity at the Citation aircraft mid-spiral height and location at several times during each spiral. We use the EDOP and S-pol data for the 980905 spiral, the S-pol radar data for 990217 and 990219, the ARMAR data for 990819 and 990830, and the Kwajalein radar data for 990822, 990823 and 990911. The changes in the mean radar reflectivity values, shown in increments of 5 dBZ$_e$ in the last column of Table 2, were generally 5 dBZ or below. As shown in Section 4, changes in dBZ$_e$ of about 5 dBZ$_e$ correspond to changes in the ice water content or precipitation rate by a factor of about two. This change is modest and therefore we conclude that the spiral descents provide not only an indication of the evolution of the PSD in the vertical but an indication of the approximate properties in the vertical over the time periods of the spirals.

There was also considerable horizontal inhomogeneity over the course of the various loops of the spirals, and the variability ($\pm$1σ bounds) about the mean values of measured dBZ$_e$ in Fig. 2 (left panels) was also often 5 dB.

C. Particle Size Distribution Properties in the Vertical

In KWAJEX, the rate of descent of the Citation coincided roughly with Doppler radar-measured particle fallspeeds. The particles dominating the measured reflectivities were

presumably at the larger end of the PSDs and their evolution in the vertical was therefore captured by the Lagrangian spiral descents. However, evolution in the small end of the PSDs was not captured although aspects can be inferred from changes in the size distributions.

PSDs averaged over various loops for the spiral of 990819 are plotted in Fig. 3. The 2D-C and HVPS data overlapped reasonably well at about 0.2 cm, thus providing nearly continuous PSD measurements for particles from tens of microns in size to centimeters. Most particles were below 0.2 cm. For particles above 0.04 to 0.06 cm, the concentrations (plotted on logarithmic axes) decreased linearly with size (linear axes), indicating that at sizes above 0.04 to 0.06 cm, the PSDs were exponential. Below 0.04 to 0.06 cm, the PSDs were linear when plotted on logarithmic axes, indicating that particle concentrations in this part of the distribution were distributed by a power-law. The maximum particle size increased downward until the ML, then decreased below as a result of melting.

PSDs plotted as in Fig. 3 do not capture the horizontal and vertical variability observed during the spirals. We developed a different type of plot to capture these trends. The left panels in Figs. 4 and 5 show height/time cross-sections of dBZ_e along the tracks of the DC-8 (KWAJEX) and ER-2 (LBA) as these aircraft flew near to and over the Citation. The boxes in the panels depict approximate locations of these overpasses *if they had occurred over a period of about two minutes* , for reference purposes only, but in fact they occurred over a thirty or so minute period (Table 2). The right panels show color-coded renditions of the PSDs during the spirals. Composite PSDs, as in Fig. 3, were color-coded to denote concentration per unit diameter, $N(D)$, with higher N in red and lower N shown in blue. Colors represent $N(D)$ (the color key is at the right), and the D scale is along the abscissa. The spirals used in Figs. 4 and 5 were selected because they contained both reliable $N(D)$ information and coincident radar data. An exception is the 990217 spiral (bottom panel, Fig. 5), where some loss of PSD information occurred because of a probe malfunction.

Inspection of the right panels in Figs. 4 and 5 shows the presence of cyclical fluctuations, indicating horizontal variability. This conclusion is supported by the radar imagery in the left panels, which indicates horizontal variability within the Citation domain sampled, sporadic bright band signatures, embedded convection, and distinct fallstreaks. It is, therefore, not necessarily meaningful to infer particle growth from loop averages for PSDs, and there are questions related to whether horizontal inhomogeneity is atypical of tropical stratiform precipitating regions and anvils and if the observations are representative of tropical cloud layers.

Beginning at cloud top, particles as large as 2 mm (990911) to 6 mm (990819, 990830) were observed. The sizes of the largest particles in the PSDs increased downward, a fea-

ture shown by the decrease downwards in the width of the dark blue color in the right panels of Figs. 4 and 5. Fig. 6 shows images from the HVPS probe for each of the 14 loops of the Citation as it spiraled from cloud top to base on 990822. The particles shown for the first few loops were at most a few millimeters in size and reach up to 1 cm in diameter during the lower loops.

The diameters of the largest particles increased downward at 0.1 to 0.3 cm km^{-1}, with lesser increases for the colder cases and greater increases for the warmer cases. As the Citation descended at a rate similar to the fall velocity of the largest particles, the broadening of the PSDs can be attributed to growth of the larger particles and not to size sorting. Although large particles could have been injected into the lower levels, giving the illusion of growth, the measured dBZ_e profiles adjacent to the spiral locations do not suggest the presence of nearby sources of large particles. However, on 990822, the proximity to convection may suggest local sources of particles.

The concentrations of small ice particles, which dominated the total concentration N_T, were greater near cloud top but generally decreased appreciably downward in the cloud (Fig. 7). Aggregates, examples of which appear in the lower panels of Fig. 8, were almost certainly responsible for the preponderance of this decrease, although a portion of the decrease may have been the result of sublimation and size sorting.

The PSDs changed markedly through the ML (Figs. 4 and 5: 990819, 990830, and 990911 spirals). The tops of the ML—marked with "0C, " in these figures for the 990819, 990830, and 990911 spirals —occurred at about 4.5 km. The size of the largest particles, D_{max}, initially increased from about 1 to 1.5 cm, while the N of particles under 0.5 cm decreased significantly (see Figs. 4, 5, and 7). Aggregation in the upper parts of the ML accounts for these observations. [2] The bases of the ML, as defined by the height at which the sizes of the largest particles no longer changed appreciably, occurred at about 3°C (3.95 km), where the largest raindrops were 0.3—0.4 cm.

D. Particle Habit Variations in the Vertical

The CPI provided information on how the particle habits varied in the vertical and the relationship of these to the measured reflectivity structures shown in Figs. 4 and 5. This instrument is best suited for characterizing the habits of the particles smaller than 2 mm; larger particles are not detected as its sample volume is too small to sample the larger particles. On 990819 (as shown in Fig. 8), numerous vapor-grown crystals were observed in

[2] Some decrease in the total concentration could have been caused by the smaller particles decreasing in size below the 2D-C detection threshold, by melting resulting in increased fall velocities and decreased concentrations or by evaporation of the small drops by preferential deposition of condensate on the larger ice particles. Calculations indicate that these were not significant factors.

the intermediate (400 to 600 μm) and large (>800 μm) sizes—including columns, capped columns, hexagonal plates, and branched crystals—whereas the habits of the small (<100 μm) particles were not identifiable. Aggregates, with some riming in the larger sizes, were also observed, especially just above and near the top of the ML. No supercooled liquid water was detected. The presence of the bright band for this spiral (top left panel, Fig. 6) indicated that updrafts were weak (because strong updrafts would disrupt the bright band). Weak updrafts are conducive to growth primarily through diffusion rather than riming. Radar echo—top heights of 8 to 9 km (from T —20 to —25°C) led to the initial formation of columns, then of capped columns as particles fell through the planar-crystal growth regime where T ranged from —12 to —18°C. In contrast, particles observed on 990822 (shown in Fig. 9) were rimed in the intermediate and large sizes with some aggregates evident, and these appeared more spherical in the small sizes. Measured radar reflectivities (Fig. 4, middle left panel) and V_Z (not shown), from which vertical velocities above a few m s^{-1} could be assessed, indicated the presence of deep updrafts, which led both to extensive riming and to complex crystal shapes often associated with the freezing of cloud droplets at low temperatures.

The relationship between particle habits, the measured radar reflectivities, and the proximity to convection was also observed in the other cases. The deep anvil generated from nearby deep and extensive convection on 990217 (Fig. 5, lower left panel, and EDOP data, not shown) produced complex, rimed crystals and aggregates of rimed crystals (upper panels, Fig. 10). No supercooled liquid water was measured on 990217, thus, riming must have been acquired in the convective regions, then particles were advected into the anvil. Conversely, for the poorly organized and weak updrafts associated with the 990823 spiral (lower panel, Fig. 4), habits consisted of pristine cirrus—type crystals (e.g., unrimed side planes and bullet rosettes), reflecting the low cloud—top T, and capped columns, reflecting additional growth around —15°C.

E. Derived moments of the size distributions

Various bulk properties were computed from the PSDs, including the ice water content (IWC), precipitation rate (R), radar reflectivity factor (Z), radar reflectivity assuming equivalent water spheres dBZ$_e$, and mean mass and reflectivity-weighted particle terminal velocity (V_m, V_Z), as in Heymsfield (1977). In this subsection, we present calculations of these parameters

1. Estimation of Ice Particle Density and Mass

Calculation of each of these variables depends on a knowledge of the ice particle density and mass as a function of D, and a knowledge of the terminal velocity (V_t), which are needed to calculate R, V_Z, and V_m. The V_t, in turn, depends on m, the ice particle cross-

sectional area (A) normal to its fall direction, and the drag coefficient. Obtaining the area is straight-forward; A was measured directly by the 2D and HVPS probes, which were oriented to measure the particles' horizontal cross-sections.

Calculation of m is more problematic. Mass is obtained from the general relationship:

$$m = \frac{\pi}{6}\rho_e D^3, \tag{1}$$

where ρ_e is the effective density (particle mass divided by the volume of a circumscribed sphere). No direct measurements of IWC were available from the TRMM observations to constrain the estimates of ρ_e, and the ARMAR and EDOP measurements were not sufficiently collocated with those of the Citation to constrain the calculations from the radar reflectivity. Although ρ_e can be estimated for some particles with pristine habits, little direct information could be ascertained for the more complex, rimed, and aggregated particles. A comprehensive study was used to estimate ρ_e, encompassing a combination of calculations, ARMAR observations, and observations of ice particle terminal velocities at the surface; we describe this effort in Appendix B. The following relationship was developed from this analysis and from the work of Heymsfield et al. (2002), hereafter H02:

$$\rho_e = k(A_r)^n D^\alpha, \tag{2}$$

where A_r is the area ratio $\frac{A}{(\pi/4)D^2}$ (number of shadowed 2D-C or HVPS pixels divided by the number of pixels in a circle with the same D), $k = 0.04$, $n = 1.5$, and α = -0.5 (cgs). The A_r provided some information about ρ_e (see H02) and the D dependence accounted for observations that the ρ_e for aggregates generally decreases with D. Although this relationship fit a number of observational data sets (described in Appendix B), the variability in ρ_e can nevertheless be large. We infer that using Eq. (2) with these coefficients provides an accuracy of $\pm$50% of the true IWC, as ascertained by comparing values for dBZ_e ($\propto m^2$) as calculated from the PSDs with those measured by the ARMAR on the same days during KWAJEX. An optimistic uncertainty in the mean ρ_e of $\pm$ 25% leads to the following approximate uncertainties: IWC, $\pm$ 25%; R, $\pm$ 45%; dBZ_e, $\pm$ 10% (for positive dBZ_e); V_Z, $\pm$ 12%; and V_m, $\pm$ 15%. We have not accounted for Mie scattering effects in these estimates; this effect minimally impacts the calculations at the ARMAR and EDOP wavelengths (Robert Meneghini, private communication).

2. Derived IWCs and other moments

Vertical profiles of IWC, Z, V_m and V_Z as calculated from the PSDs for three spirals (shown in Fig. 11) were selected as representative of the findings for the ice regions of all spirals. The equations used to calculate these properties are presented and parameterized

in section 4C and listed in Table 3. The calculations are derived for temperatures 0°C and below to avoid ambiguities associated with particle mass in the melting layer. Our main findings were as follows:

1 The magnitudes of the IWCs are mostly from 0.1 to 0.5 g m^{-3}, and change by only about a factor of two or three with height, much less than is observed for synoptically-generated ice clouds over comparable vertical depths (see Section 5 and Fig. 18). The horizontal variability noted in the IWC values of less than 50% during the course of a spiral is comparable to that observed in earlier Lagrangian spiral descents reported on by Lo and Passarelli (1982) and Field (1999). The magnitudes of the IWCs, and associated calculated values for dBZ_e, were comparable to those for mid-latitude anvils (Heymsfield 1986).

2 The precipitation rates changed by less than a factor of two over the course of the various loops of each spiral and by less than a factor of three over the cloud depths, with the exception of the 990822 case. This result is good given that our goal was to sample the same population of particles as they fell from upper to lower cloud levels, implying a nearly constant R with height.

3 The trends of calculated dBZ_e with height differed markedly from the radar observations, shown in Fig. 2. This is not surprising given that the radar data were acquired over only part of the Citation track and for a very limited portion of each spiral. The calculated peak values of dBZ_e, however, were comparable to the radar measurements. Mie scattering effects should be included in cases where calculations and measurements of dBZ_e can be made directly.

4 The V_m were of the order 1 m s^{-1}, very reasonable for the calculated IWCs and Rs.

4. PROPERTIES AND PARAMETERIZATIONS OF THE PSDs

The focus of this section is to develop general relationships for the PSDs, and between the PSDs and various microphysical and radar-measured properties for use in cloud–resolving models, climate models, and remote-sensing applications.

A. Form of the Ice PSDs

In this subsection, we use curves fitted to the PSDs to quantify how the PSDs from the Lagrangian spirals varied with temperature and height, and to quantitatively assess how horizontal variability influenced the PSD. Not all spirals were used in this analysis, because a complete set of 2D and HVPS data was not always available.

Based on the work of Kosarev and Mazin (1991), Mitchell (1991) and others, gamma distributions of the form

$$N = N_{0\Gamma} D^{\mu} e^{-\lambda_{\Gamma} D} \tag{3}$$

were fitted to the PSDs with diameters 66 μm or two 2D-C probe size bins and above for each 1 km of horizontal distance, or about 20 m in the vertical and 8–9 sec of flight. The intercept ($N_{0\Gamma}$), slope (λ_{Γ}), and dispersion (μ) values were derived for each PSD by matching three moments (Kozu and Nakamura 1991; Zhang et al. 2001). We have chosen to use the first, second, and sixth moments, as this set provided the best fit over the entire measured particle size range. (Symbols in the discussion that follows are defined in Appendix A.)

The fit coefficients were derived as follows. The pth moment $M(p)$ of the observed PSD is given by

$$M(p) = \int_0^{D_{max}} p(D) D^p dD. \tag{4}$$

The parameter μ can be derived by finding the only real root of the quartic polynomial

$$(1-F)\mu^4 + (8-18F)\mu^3 + (24-119F)\mu^2 + (32-342F)\mu + (16-360F) = 0, \tag{5}$$

where $F = \frac{[M(2)]^5}{[M(6)][M(1)]^4}$. The other fit parameters are derived from

$$\lambda_{\Gamma} = \frac{M(1)(\mu+2)}{M(2)}, \tag{6}$$

and

$$N_{0\Gamma} = \frac{M(1)\lambda_{\Gamma}{}^{(\mu+2)}}{\Gamma(\mu+2)}. \tag{7}$$

This method produces a fit that is also in good agreement with other moments that are not used in the fitting routine, such as the third moment, used for computing IWC. Also fitted were exponential curves ($\mu = 0$) in Eq. (3)), for reference to earlier studies. Hereafter, the fit coefficients for the exponential will be noted by λ and N_0, and for the gammas by λ_{Γ}, $N_{0\Gamma}$, and μ.

The values of λ and λ_{Γ} obtained for the various spirals showed a correlation with T (Figs. 12A and 12B) and with each other (Fig. 13A), although there was considerable variability. The λ and λ_{Γ} values were about the same (Fig. 13A), except below λ and λ_{Γ} less than 15 cm^{-1} and above λ and λ_{Γ} greater than 70 cm^{-1}. The solid line in the figure (and the fitted equation) shows where the values deviate.

For $T \leq$ —15°C, the λ and λ_Γ values were usually greater than 20 cm^{-1}, with the exception of the 990822 case, which differed, presumably because of the proximity of the sampling to convection and possibly because it was an anvil. For values of T between -5 and -15°C, the λ values decreased to between 12 and 20 cm^{-1} while the λ_Γ were somewhat lower. As T increased toward 0°C, the λ values were asymptotic at 8 to 10 cm^{-1}, similar to findings in earlier studies (Houze et al. 1979; Lo and Passarelli 1982), which indicated that λ values did not decrease below 8 to 10 cm^{-1}. The λ_Γ values below approximately 4 cm^{-1} resulted from poor curve fits, as ascertained from the correlation coefficients for the curve fits.

For individual spirals, the λ versus T values and the λ_Γ versus T curves fell along nearly straight lines, with slopes ($\frac{d\lambda}{dT}$ or $\frac{d\lambda_\Gamma}{dT}$) that were within a factor of 2 of each other over all cases. Within loops of individual spirals, the λ or λ_Γ values usually fluctuated by at most $\pm$ 50%, far less than the changes noted over the course of a spiral (see insert, Fig. 12B). The λ values conformed quite closely to the λ equation from Ryan (2000) for mid-latitude ice clouds that has been converted to an exponential form here,

$$\lambda \ (\text{cm}^{-1}) \ = \ c_0 \exp^{(c_1 T[\text{C}])}, \tag{8}$$

where the c_0 and c_1 values adapted from the coefficients in Ryan are are 12.1 cm^{-1} and —0.0564, respectively, and the curve is plotted in Fig. 12A. Coefficients c_0 and c_1 were derived from fits to the median TRMM values of the distribution of λ versus T and λ_Γ versus T shown in Figs. 12A and 12B, along with curves fitted to the $\pm$ 1σ values. (The data from the outlying 990822 case was omitted from the fitted data set, and two curves were fitted to the λ_Γ versus T data). Curves representing these equations are plotted in Figs. 12A and 12B and are listed at the bottom of Table 3. In and below the ML, λ and λ_Γ values again increased, in much the same way as was shown for λ values by Houze et al. (1979).

We can assess how accurately T would have predicted λ_Γ by using the TRMM temperatures in the spirals and comparing the predicted to measured λ_Γ (Fig. 13B). As is shown in the figure, this approach to predicting λ_Γ leads to considerable scatter, especially for the outlying case on 990822, where virtually all of the points deviate widely from the line in Fig. 13B—thus, T is not an ideal predictor of λ_Γ (or λ) values. A similar interpretation results if the Ryan (2000) relationship is used to estimate λ.

The N_0 and $N_{0\Gamma}$ values also decreased systematically with increasing T (Figs. 12C and 12D). However, there is no strong dependence of N_0 or $N_{0\Gamma}$ on T, which is why Ryan (2000) also found no clear relationship between N_0 and T, only noting that "the parameter N_0 is a less systematic function of T with local geographic variations being evident.". Furthermore, there is considerably more scatter than was found for λ and λ_Γ especially over

individual loops, where N_0 or $N_{0\Gamma}$ often varied by up to one or two magnitudes (insert, Fig. 12D). Since IWC is proportional to N_0 and $N_{0\Gamma}$ (Section 4C), the variability of the N_0 and $N_{0\Gamma}$ represents IWC variability, and indicates that there are large fluctuations in IWC across the loops of the spirals.

The correlation coefficients (r) for the exponential fits (Fig. 12E) were generally high for T values between -35 and -5°C but not outside of this range. For λ values above 80 cm^{-1} or below 15 cm^{-1}, the quality of the exponential curve fits decreased. Nevertheless, the r value averaged over all exponential fits was 0.96, signifying that the exponential fits were quite good. The gamma distribution fits produced even better correlation coefficients (not shown) with an average r value of 0.98, and eliminated the problem areas at high and low λ.

At the larger values of λ_Γ , the μ tended to have positive values (subexponential distributions), whereas at the lower values of λ_Γ μ had negative values (Fig. 13C) (superexponential distributions). Fluctuations in the μ values during the loops of individual spirals were of order of 1.0 (insert, Fig. 12F), signifying that there was considerable variability in the shape of the PSD in small sizes. The μ values were close to -1 in the range $25 < \lambda < 70$ (Fig. 13C), which is why the correlation coefficients for the exponential were relatively high in this range. The exception was noted on 990822, where μ values fell below -1.

The values of μ were highly correlated with both λ_Γ and $N_{0\Gamma}$ (Figs. 13C-D), especially below 0°C. The curve fits shown in these figures and listed at the bottom of Table 3 can be used to eliminate the $N_{0\Gamma}$ term in Eq. (3) and reduce the number of unknown variables in Eq. (3) to two. The fits were derived with and without the data for the 990822 case, with little difference found.

An indirect relationship was found between the maximum measured particle size, D_{max}, and λ or λ_Γ (Fig. 14). [3] At least two particles were required in a given HVPS size bin to find a D_{max}. The D_{max} at high λ or λ_Γ (low T) values were several millimeters and at low values were 1 cm or above. Curves fitted to the mean and standard deviation values are indicated in the figure and listed at the bottom of Table 3, with little difference found with and without the inclusion of the 990822 data. Extrapolation of the D_{max} curve in Fig. 14A to 2 cm or above returns λ values of only 6 or 7 cm^{-1}. We speculate that the absence of λ values of less than 8 or 9 cm^{-1} in earlier studies is due to a rarity of aggregates larger than 2 cm.

[3] Decreasing λ or λ_Γ values and hence increasing spectral breadth will generally lead to an increase in D_{max}. The measured D_{max} also depends on the probe sampling volume and N_0 or $N_{0\Gamma}$ (which displace the PSDs upward or downward), and this relationship embodies these factors implicitly.

The N_0 and λ or $N_{0\Gamma}$ and λ_Γ values were highly correlated for individual spirals (Figs. 15A and 15B) and tended to decrease from large values at the top of the spirals to small values in the upper parts of the ML (indicated by $\circ$ in each panel). Broadening of the PSDs with distance below cloud top by aggregation and with a corresponding decrease in N_0 or $N_{0\Gamma}$ by depletion of the smaller particles can account for this trend, although there are issues related to whether evolution of small particles was actually being observed during the Lagrangian spirals. The increase in D by diffusional growth is very slow for large particles even if the environment was supersaturated with respect to ice and cannot account for these observations.

The 0°C level was denoted by a marked change in the trend of the N_0 versus λ or $N_{0\Gamma}$ versus λ_Γ points with T (Figs. 15A and 15B). Between 0 and 1.5°C, corresponding to the first several hundred meters, the λ or λ_Γ values decreased slightly, reflecting slight increases of D_{max} and decreases in the total crystal concentration (Figs. 4 and 5; 990819, 990830, and 990911 cases). Broadening in the large end of the PSDs is consistent with previous observations by Yokoyama (1985) and Willis and Heymsfield (1989), who reported that aggregational growth continued several hundred meters into the ML. The decrease in N_0 or $N_{0\Gamma}$ is only partially accounted for by ice particles melting to sizes below the 2D-C detection threshold because particles of sizes of 50 μm and below have high densities and do not change their D values much by melting. Most of the decrease is attributable to depletion by aggregation.

The lower part of the ML was characterized by an increase in the N_0 and $N_{0\Gamma}$ values (from the $\circ$ to $\triangle$ symbols in Figs. 15A and 15B). These increases suggest that there is little breakup of partially melted individual aggregates to multiple particles in this region, as the total concentration, from $N_t = \frac{N_0}{\lambda}$, (for an exponential, Sekhon and Srivastava 1970), remained essentially constant. The increases in the λ or λ_Γ values in the lower part of the ML resulted from a dominance of melting by the larger, lower—density aggregates. At this height in the ML, most of the smaller ice particles have melted, thus, their size is basically unchanged. The diameters of the larger, relatively low—density aggregates changed significantly. Thus, the λ and N_0 or λ_Γ and $N_{0\Gamma}$ values increased slightly.

B. Parameterizations of the Ice Particle Shapes

The area ratio is an important property in our estimates of ice particle density given by Eq. (2) and in parameterizing area-related properties (terminal velocity, extinction) of the PSDs. The A_r is expressed as a power-law function of D: $A_r = aD^b$. The coefficients a and b can be derived through curve fits to the A_r versus D data from the imaging probes, collected over 1-km intervals during the spirals. As shown in Figs. 16A to 16D, the a and b coefficients are a strong function of altitude and temperature, and not sur-

prisingly tend towards spheres (a =1, $b = 0$) in the melting layer. The height trends conform to the tendencies found for midlatitude cirrus clouds by Heymsfield and Miloshevich (2002), who attributed the changes in height or temperature to aggregation and sublimation. Points for the 990822 case, shown as grey symbols in Fig. 16, differ somewhat from those for the other cases. Given that the λ values decrease downwards, it can be inferred that the height and temperature tendencies are consistent with changes in λ. This result is confirmed in Fig. 16E, which shows the changes in the coefficient a with λ. A nearly monotonic relationship is found between b and λ, or between a and b (Fig. 16F), with relatively little scatter. Curve fits between a and λ, and a and b, are shown in Table 3, both to the mean values and standard deviations to indicate the extent of the scatter in the values.

C. Parameterizations of the Moments of the PSDs

The set of equations used to calculate the bulk properties of the particle population, including the IWC, R, Z, V_m, V_Z, the extinction coefficient, ϵ, and the effective radius, r_e, are shown in Table (3), with the symbols identified in Appendix A. They use as input the values from the relationship between the various properties of the gamma distributions and temperature reported in Section 4A; these equations are listed at the bottom of Table 3. The equations make use of PSDs represented by gamma distributions (Eq. 1) which provides an accurate representation of the TRMM PSDs, although they can readily use exponential if the value of μ is taken to be 0. The equations listed under "Full Equations" in the table are general and can use many of the earlier measurements of the properties of exponential size distributions for ice particles reported later in Section 5.Particles below the 2D-C probe detection threshold are included implicitly through the use of the gamma distributions, but the accuracy in these sizes cannot be estimated. The resulting errors might have a major affect on the lower moments (primarily on total concentration and cross-sectional area) of the distributions but not on the higher moments (IWC or dBZ_e).

The IWC can be expressed as

$$\text{IWC} = \frac{\pi}{6} k N_0 \int_0^{D_{max}} {A_r}^n D^{(3+\mu+\alpha)} e^{-\lambda D} dD, \tag{9}$$

using the coefficients α, k, and n identified in section 4A and at the bottom of Table 3. The resulting solution to the integral of Eq. (9) is shown in column 2 of Table 3 for integration from 0 to ∞ (complete gamma function). We also integrated this equation over the range 0 to D_{max} (incomplete gamma function), with a generic solution shown at the bottom of the table. For given $N_{0\Gamma}$ and λ_Γ values, IWCs returned from the complete and incomplete gamma functions differed insignificantly. A simplified relationship derived using the values of α, k, and n are presented in column 3.

The relative accuracy of the estimates of IWC using the exponential and gamma PSDs is shown in Figs. 17A and 17B. The numerators given in each of these panels were derived by taking the IWCs, as calculated from Eq. (9), using the fitted N_0 and λ or $N_{0\Gamma}$ and λ_Γ values and the TRMM average A_r versus D relationship. The denominators are the IWCs derived directly from the PSDs and measured A_r values. Using exponential size distributions to derive IWC values leads to significant departures in the ratios from unity. Dramatic improvements were noted through the use of gamma distributions, yielding values generally close to unity. Therefore, the gamma distributions provide a much better representation of the PSDs than do the exponential.

If IWC is known from measurements or prognosed in a general circulation model (GCM), the corresponding N_0 and λ or $N_{0\Gamma}$ and λ_Γ values can be readily found. The relationship between λ and T or λ_Γ and T at the bottom of Table 3 can be used to prescribe λ or λ_Γ ; given an IWC, N_0 or $N_{0\Gamma}$ values can then be obtained from the IWC relations shown in Table 3. This technique is illustrated in Fig. 17C: λ_Γ values are derived from T (bottom, Table 3); the $N_{0\Gamma}$ values and μ values are taken directly from the gamma fits; and then the IWC is calculated. The ratios of the calculated IWC values to the values taken directly from the PSDs may then be derived. In essence, this method tests for the error that can be expected in $N_{0\Gamma}$ when IWC and T are known. The grouping of points near the bottom of the panel actually represents data points and shows that for the 990822 case this method greatly underestimated the IWCs because the λ_Γ values were overestimated. For points for the other spirals the scatter is large but the method is generally accurate to $\pm 50\%$. Use of the exponential (not shown) produces larger errors because the population of small particles is inaccurately prescribed by the exponential. More accurate estimates of N_0 or $N_{0\Gamma}$ are not possible without better understanding of the factors responsible for the variability in λ or λ_Γ .

The median mass diameter, D_{mm}, a property related to the distribution of ice mass with size, can be found by modifying the results presented in Mitchell (1991) and is a function of λ_Γ, μ, and the coefficients in the exponent of D in Eq. (9). The equation is presented in Table 3.

The radar reflectivity (Z) can be calculated from

$$Z = \int_0^{D_{max}} N(D) {D_m}^6 dD, \tag{10}$$

where D_m is the melted equivalent diameter, found using the expression for ρ_e as given in Eq. (2). Equation (10), for Z, is analogous to Eq. (9) for IWC, with the results shown in Table 3. Wavelength-dependent, Mie scattering effects were not considered in the integral evaluation. As with IWCs, the gamma distributions provide a better match to the

values calculated from the PSDs than do the exponential (see Figs. 17D and 17E). Given values for Z and T, N_0 or $N_{0\Gamma}$ can be found in a similar manner to that described for calculating IWC. However, this method may lead to very large errors (Fig. 17F). The equivalent radar reflectivity dBZ_e listed in Table 3 is derived assuming equivalent water spheres (Smith, 1984).

The precipitation rate (R) was calculated by incorporating the following A_r-dependent V_t relationship from H02 inside the integral in Eq. (9):

$$V_t = a_f(\frac{4gka^{n-1}}{3\rho_a})^{b_f}\nu^{(1-2b_f)}D^{[(3+b(n-1)+\alpha)b_f-1]} = CD^{\kappa}, \qquad 11$$

where ν is the kinematic viscosity of air, ρ_a is the density of air, and a_f and b_f are the coefficients used in fall velocity relationships of the form introduced by Mitchell (1996) and recently modified by H02 to account for aggregates. To solve Eq. (11), only one set of a_f and b_f coefficients can be used at this time to represent all sizes. We carefully examined the use of appropriate a_f and b_f coefficients, and selected those shown in Table 3. The integrated equations for R appear in Table 3.

Equations for V_Z and V_m also follow the development used for Eqs. (9) and (11). The V_t given by Eq. (11) is included in the integral in Eq. (9) and normalized by the IWC to obtain V_m; V_t in Eq. (11) is incorporated in the integral in Eq. (10) and normalized by Z to obtain V_Z. Solutions of these equations appears in Table 3. Note that these fall-velocity expressions do not depend directly on N_0 but do depend on μ and thus indirectly on N_0. Also note that different sets of the a_f, b_f coefficients are used for V_m and V_Z resulting from different parts of the PSD contributing to each. The V_m equation predicts values that are accurate to $\pm 20\%$ (mostly slight overestimates) for D_{mm} above 0.03 cm (>90% of the points) and the V_m equation predicts values that are accurate to $\pm$ 20% for D_{mm} from 0.02 to 0.2 cm (83% of the points).

Given V_Z and Z values, the V_Z expression can be used to derive λ_Γ , $N_{0\Gamma}$, and μ values. With the use of Z or IWC, the full properties of the exponential PSDs are known. Vertically-pointing Doppler radar data, with some time averaging to remove small-scale vertical motions [4] , can therefore be used to obtain direct measurements of λ_Γ and N_0 without the need to make assumptions about the temperature dependence of λ_Γ .

The total cross-sectional area of a population of particles (A_c) is given by

$$A_c = \frac{\pi}{4}\int_0^{D_{max}} N(D)A_rD^2dD, \qquad (12)$$

[4] It may not be possible to remove vertical velocities of order 10 cm s^{-1} associated with the melting layer and synoptic systems by averaging over long periods of time

and the extinction coefficient in visible wavelengths (when particles are large compared to the wavelength) is calculated from $\epsilon = 2A_c$. Solutions for these integrals are listed in Table 3, where the a and b coefficients can be taken directly from either the relationship to λ shown in the bottom of Table 3 or from the average values of each coefficient listed in the table.

The effective radius (r_e), a parameter that characterizes the radiative size of a population of particles, can be written, according to Fu (1996), as

$$r_e = \frac{\sqrt{3}}{3\rho_i}\frac{\mathrm{IWC}}{A_c}, \tag{13}$$

where $\rho_i = 0.91$ g m^{-3}. Solution of this equation derives from Eqs. (9) and (12) and is given in Table 3. For the TRMM spirals, the absence of measurements from small particles is not thought to significantly affect the r_e values. Heymsfield and McFarquhar (1996), who did have measurements of size spectra down to about 10μm in size, showed that the r_e at the warmer temperatures in tropical anvils were dominated by the larger particles.

5.DISCUSSION

Lagrangian spiral-type descents and ascents have been used previously to examine the evolution of PSDs in mid-latitude layered and frontal clouds by Passarelli (1978), Lo and Passarelli (1982), Gordon and Marwitz (1986), and Field (1999) (hereafter P78, LP82, GM86, and F99, respectively). In these studies, values for T at cloud top (-30°C) and base (2°C) were comparable to those of the TRMM observations. PSDs were measured using 1D-P (P78, LP82); or 2D-C and 2D-P (GM86); or the 2D-C and HVPS probes (F99). Diffusional and aggregational growth predominated in each of the spirals.

The parameters N_0 and λ of the exponential fitted to their PSDs by each of the authors are plotted in Fig. 18. More scatter was evident in the N_0 versus λ values than we found for the exponential in our spirals because the probe sample volumes and upper size detection limits in all but the F99 study were significantly smaller than those used in our study. For reference, the T values at cloud top and base are shown in each panel, and the approximate envelope of the N_0 versus λ values from the TRMM observations are given in the lower right panel. Also plotted in two of the panels are the λ values derived from the measured T from the TRMM observations (bottom of Table 3).

The following similarities and differences may be noted between these and the TRMM observations as shown in Fig. 15A:

1. The λ values generally fell in the range 10 to 50 cm^{-1}, similar to the TRMM observations over the same T range.

2. The trends in the N_0 versus λ values were similar to those we observed. One of the GM86 and two of the LP82 cases first showed an increase in the N_0 value with a decrease in the value of λ at cloud top. This pattern was attributed by the authors to particles growing by diffusion into the size-detection threshold of the 1D-P and 2D-C probes and to ice nucleation.
3. The TRMM parameterization does a reasonably good job of predicting the value of λ when λ decreases with T, at T below 0°C, and when sublimating bases are not present.
4. The N_0 values for most but not all cases were comparable to the TRMM N_0. Above 0°C, N_0 values for the two GM86 cases and those from the TRMM observations corresponded closely. It is in this region that the probe sampling volume issues are probably minimized. Values for N_0 for several of the LP82 and P78 cases were below those measured during TRMM. We believe that this results from an underestimate of the concentrations of crystals in the smaller size range of the 1D-P, a conjecture confirmed by comparisons in GM86 of N_0 values from the 2D-C and 2D-P probes. As reported in GM86, the ratio $N_0(2\mathrm{D}-\mathrm{P})/N_0(2\mathrm{D}-\mathrm{C}) = 0.21$, whereas the ratio $\lambda(2\mathrm{D}-\mathrm{P})/(2\mathrm{D}-\mathrm{C}) = 0.72$; thus, N_0 changes appreciably but λ doesn't.
5. The range of IWCs sampled from these various spirals was comparable to those from the TRMM spirals. The lines of constant IWC in Fig. 18 were derived from $\mathrm{IWC(g\ m^{-3})} = \frac{\pi}{6}\frac{\mathrm{N_0 y\Gamma(4+\eta)x10^6}}{\lambda^{(4+\eta)}}$, which comes from Sekhon and Srivastava (1970), with y=0.0056 and η=—1.1 taken from Brown and Francis (1994). For a given constant value of IWC and a value of λ, N_0 values were derived and the lines of constant IWC were plotted.
6. Most importantly, the gamma functions would have provided better estimates of the PSDs for λ below 20 to 30 $\mathrm{cm^{-1}}$.

Sekhon and Srivastava (1970) derived the following relationships for snowfall collected at the ground:

$$N_0 = 2.50\mathrm{x}10^{-2}R^{-0.94}\ (\mathrm{cm^{-4}}),\quad \lambda = 22.9R^{-0.45}\ (\mathrm{cm^{-1}}), \tag{14}$$

where N_0 and λ are for the resulting melted PSDs. Although no direct relationship between N_0 and λ was derived, this relationship can be estimated by eliminating R in Eq. (11), yielding

$$N_0 = 3.61\mathrm{x}10^{-5}\lambda^{2.09}. \tag{15}$$

We could have developed a more accurate relationship than that given by Eq. (15) if the original N_0 versus λ data points were available. In Fig. 19, Eq. (15) is plotted over the

range of R reported in that study. Also shown in the figure are the N_0 versus λ points for the 990822 spiral and the corresponding "melted" N_0 versus λ points. These were obtained by fitting exponential curves to the concentration versus melted equivalent diameters (from ρ_e in Eq. [2])for each PSD.

Our melted N_0 versus λ points differed somewhat from points along the curve given by Eq. (15), possibly for the following reasons. At T above approximately —5°C, the λ values for the unmelted and partially melted spectra remain relatively constant at 9 cm^{-1}. This regime could not be discerned from the small number of points used in the Sekhon and Srivastava analyses. Furthermore, partially melted snow and/or raindrops were included in about half of the samples. Inspection of Fig. 11 shows that for a narrow range of T values between 0 and 3°C (for each spiral within this range, the R values were approximately constant), the λ values varied by a factor of 2-2.5. Thus, for partially melted snow, there is no unique R versus λ relationship, and the data points within the region of melting are suspect.

McFarquhar and Heymsfield (1997) (hereafter MH97) recently developed a parameterization for the PSDs of tropical ice clouds (produced by outflows of deep convection) as functions of T and IWC, with stated ranges of validity -70 $\leq$ T $\leq$ -20 °C and for 10^{-4} $\leq$ IWC $\leq$ 1 g m^{-3}. The intention of McFarquhar and Heymsfield was to produce reliable measures of both IWC and cross-sectional area. The authors emphasized in this paper the small particles that often dominate cloud extinction and optical depth. The PSDs, which were measured from about 10 μm to a size larger than 1 mm, depending on the particle concentration (Table 1), were converted to $N(D_m)$ for $D_m \leq 1000$ μm through use of mass-diameter relationships. They were then represented as the sum of a first-order gamma function, describing ice crystals with $D_m \leq 100$ μm, and a lognormal function, describing larger crystals. The percentage of the IWC comprising small particles, $D_m < 100\mu$m, decreased with increasing IWC values. For IWCs of order 0.001 g m^{-3}, this portion from small particle was 80%), whereas for IWCs of order 0.1 g $^{-3}$, this fraction decreased to less than 30%.

We fitted the PSDs generated by the MH97 parameterization to gamma distributions using Eqs. (4) to (7) to permit a qualitative comparison with our observations. The range of temperatures and IWCs at which the CEPEX and TRMM observations overlapped were examined: —20 to —50°C and 0.01 to 1 g m^{-3}. Throughout this range single gamma distributions did a good job of representing the two curves used for the MH97 parameterization, reliably capturing the inflections in the curves.

It was difficult to compare the two sets of observations directly, because in MH97 the parameterization was derived in terms of the melted equivalent diameter which involved

assumptions about the particle density that differed from those made in this paper. Nevertheless, drawing upon the results of the comparison of λ and the melted equivalent λ in Fig. 19, we were able to note similarities and differences in μ and λ_Γ . Whereas our observations indicated that λ_Γ and μ were primarily functions of T, the same coefficients using the MH97 parameterization were primarily functions of IWC and only somewhat functions of T. The range of μ were comparable, -1 to 2.5, for the fits to the MH97 parameterization, whereas the λ_Γ values from the parameterization were larger than would be expected by "melting" our spectra. More direct comparisons of the CEPEX and TRMM results will be the subject of a future study.

6.SUMMARY AND CONCLUSIONS

In this study, we have examined the characteristics and evolution of the PSDs in stratiform precipitating regions and anvils during the TRMM field campaigns in Florida, Brazil and Kwajalein, Marshall Islands, emphasizing data from Kwajalein because the microphysical probes used for those observations performed better.

Cloud layers were sampled through the use of slow Lagrangian spiral descents, most of which commenced near cloud top and ended near cloud base (or at temperatures above 0°C). This flight pattern facilitated investigation of how the PSDs changed in the vertical, both within the ice regions and in the melting layer. The patterns provided information on the vertical distribution of cloud microphysical properties, although the profiles could have changed temporally in a way partially characterized using radar data over the course of the spirals. While our Lagrangian spiral descents are far from perfect in assessing the evolution of particles in the vertical and in characterizing the properties of particle size distributions because of horizontal variability and temporal evolution, we believe that the results are a step towards increasing the understanding of how tropical ice cloud properties vary in the vertical.

The use of new instrumentation, allowing more accurate measurements of the concentrations of larger particles and better definition of particle habits, has provided a data set that is more complete than has been previously available. The following summarizes the main findings.

1. Relatively large particles were measured at cloud top, from 2 mm (990911) to 6 mm (990819, 990830), even at T values as low as —50°C. Such large particles have not been observed near the tops of layer clouds in the past. Particles of these sizes fall rapidly, above 1 m s^{-1}. Rapid fallout, coupled with the particles' increased growth downward through aggregation, which will generally further increase their fallspeeds, would indicate that there is rapid transport of moisture from upper tropospheric levels to mid and lower levels.

2. With distance below cloud top, the PSDs broadened, with some particles in the upper part of the ML reaching sizes exceeding 1 cm. Aggregation, which produced this growth, also led to depletion of particles smaller 0.1 cm, conforming to the observations of Field (2000) and others of how the aggregation process works.
3. Changes in the characteristics of the PSDs were quantified through the use of gamma distributions of the form $N = N_0 D^{\mu} e^{\lambda_g D}$ fitted to the PSDs, using a technique that matches the errors in the first, second, and sixth moments of the distributions. Exponential (μ =0) were also fitted to the PSDs. From cloud top to cloud base, or the top of the ML, the $N_{0\Gamma}$ and λ_Γ values were found to decrease monotonically. A similar tendency was observed for the exponential fits, with the results showing remarkable similarity to results from earlier studies of deep ice clouds as well as of cirrus clouds. Horizontal inhomogeneities over the course of individual loops of the spirals is manifested primarily in variations in $N_{0\Gamma}$ or N_0. The μ changed systematically with height, from positive (subexponential) in the upper parts of the clouds to negative (superexponential) in the lower parts of the clouds. The $N_{0\Gamma}$ and μ values were highly correlated, and an expression developed between the two parameters eliminated one unknown in the gamma distribution form.
4. The $N_{0\Gamma}$ values first decreased by about one order of magnitude near the top of the ML, whereas the λ_Γ values decreased only slightly. Both the λ_Γ and $N_{0\Gamma}$ values then increased abruptly in the lower part of the ML until the base was reached.
5. The λ_Γ and λ values were generally a function of T, and curves were fitted to the data, although there was considerable scatter. The curve was similar to that reported by Ryan (2000) for mid-latitude synoptically and frontally generated ice clouds. We showed that the λ_Γ versus T relationship could be used to estimate $N_{0\Gamma}$ when either IWC or dBZ_e can be measured, although errors in $N_{0\Gamma}$ of up to a factor of 3 might result from this method. However, this extent of error is no worse than errors resulting from the parameterizations of the PSDs used in other studies. More accurate estimates may be possible through the use of vertically pointing Doppler radar data.
6. Exponential curves fitted to our PSDs for tropical clouds that formed in association with convective forcing had λ and N_0 values that were similar to earlier studies for mid-latitude clouds formed primarily through synoptic forcing. The monotonic relationship found between N_0 and λ or $N_{0\Gamma}$ and λ may be applicable to a wide variety of cloud types and geographical locations.
7. We developed general expressions between a number of macroscale and remote-sensing variables (e.g., IWC, Z, V_m, V_Z, R, ϵ, r_e) and $N_{0\Gamma}$ and λ_Γ . These expressions reduce to exponential if μ is taken to be zero. The free variable in these expressions is N_0, a

term that will largely compensate for variations in IWC or dBZ_e at a given temperature. Terms needed to derive the coefficients in the relationship—specifically the dependence of ice particle density on size—were derived using some new techniques. Because these expressions are general, they can be modified as new information on ice particle density becomes available.

8. It was shown that the variable V_Z is fundamentally a function of the spectral slope λ or λ_Γ. The distribution of V_Z with dBZ_e we examined in the stratiform regions in Appendix B provided implicit information on the distribution of λ and λ_Γ with dBZ_e. A similar analysis of ARMAR radar observations from three days from the TOGA COARE cirrus cloud observations, two of which appear in Heymsfield et al. (1998), show a similar V_Z vs dBZ_e pattern, suggesting that the distribution of λ with dBZ_e is similar between the two data sets.

9. Although a plethora of ice particle shapes were observed—extending all the way from complex rimed crystals and rimed aggregates to pristine particles—much of the variability could be explained by examining the Doppler radar data and quantified through use of the area ratio parameter. Rimed ice particles were sampled near deep convective clouds with sustained convection, as evidenced by the presence of deep and horizontally extensive anvils. Small (sub-mm), pristine particles were observed in clouds formed by more transient convection, with cloud-top temperatures controlling the habits: at low values of T, cirrus-type crystals, in some instances evolved into the capped columns that usually reflect growth at warmer temperatures; at high values for T, planar-type crystals and capped columns dominated. Most particles of the larger sizes were aggregates. Relationships between the ice particle area ratio and diameter were used to describe the changes in the ice particle shapes with height, temperature, and λ_Γ .

10. Our PSDs, after "melting" them to obtain equivalent water PSDs and then fitting exponential curves to them, compared reasonably well with those of Sekhon and Srivastava (1970). We surmised that any differences resulted from the few samples (only 14) that were available to those researchers to capture the λ versus N_0 dependence in the critical regime where λ values asymptote to about 9 cm^{-1}. Also, about half of their samples were collected in the ML, where no direct relationship is evident between λ and N_0 values. Although we could not directly compare our gamma size distributions to the tropical cirrus PSD parameterization represented in terms of the melted equivalent diameter for $T < -20°\mathrm{C}$ by McFarquhar and Heymsfield (1997), a cursory examination showed that these have similar characteristics. The latter parameterization is clearly superior in low-IWC regimes and at low temperatures, whereas the parameterizations we developed

are more flexible, are based on better measurements of the size distributions in larger sizes, and are better suited to the warmer temperatures and higher-IWC regimes.

11 Given the range of conditions sampled, the results of our study apply to physically thick stratiform precipitation regions and anvils with temperatures from 3°C to about —40°C. The observations apply to clouds falling into the category of "Deep Convection" according to the ISCCP optical-depth and height related cloud classification scheme. The observations also apply to the range of IWCs from 0.01 to 1 g m^{-3}, and radar reflectivities, as measured from overflying aircraft, in the range of 0 to 25 or 30 dBZ_e.

The expression that we developed between IWC and the properties of the PSD (Eq. [9]) could have been substantially improved if direct measurement of IWC had been available. With direct measurements, assumptions that had to be made about ice particle density (the coefficients k, n, and α, and their variation within the ML) might not have been necessary. Also, questions about whetherλ_Γ depends on both temperature and IWC could have been addressed. Future direct measurements of IWC—along with PSD measurements from the probes—are needed.

In closing, we would like to point out that there was considerable horizontal variability throughout most of our Lagrangian spiral descents and that the melting layers associated with four of our spirals were not horizontally extensive or homogeneous as might be the case in tropical mesoscale convective systems. A comparison of the ARMAR V_Z versus dBZ_e relationships from the KWAJEX and TOGA COARE data sets suggests that the observations apply to a broad range of tropical ice clouds. However, more tropical observations of PSD properties are clearly needed. We also want to point out that the TRMM satellite radar, which detects a minimum reflectivity of about 18 dBZ_e, would have seen some of the ice clouds we sampled on 990905 (TEFLUN-B), 990217 (LBA), 990819, and 990830 (KWAJEX). Our observations may therefore be useful in understanding the properties of the ice clouds and associated melting layers that the TRMM radar often detects.

Acknowledgments This research was supported by the NASA TRMM Project Office through grant numbers NAG5-7743 and NAG5-9715. A portion of this research was performed by Jet Propulsion Laboratory, California Institute of Technology, under contract with NASA. The authors are grateful to Martin Brown and the UND Citation crew for their help over the course of this study, and Andy Detwiler and Rand Feind for use of their software to process HVPS data. The authors also wish to thank Sandra Yuter, Sharon Lewis, and two anonymous reviewers for their thorough reviews. Thanks go to Greg McFarquhar for allowing us to use his CEPEX parameterization code, and to Beverly Armstrong for editorial assistance.

Appendix A: List of Symbols

Symbol	Description
A	Particle cross–sectional area; e.g., the particle's area projected normal to its fall
A_c	Total cross-sectional area of particle population (cm^{-3})
A_r	Area ratio–particle area divided by area of circle with the same D
a, b	Coefficient, exponent in the fit of the area ratio versus diameter data from 1-km imaging probe data
a_f, b_f	Coefficients, exponents in Mitchell (1996) and H02 Best Number versus Reynolds Number relationships
C	Coefficient in the terminal velocity relationship
c_0, c_1	Coefficient, exponent in equation relating λ to T
D	Maximum particle dimension, found by projecting its cross-section onto a horizontal plane normal to its fall direction
D_m	Melted equivalent diameter
D_{mm}	Median mass diameter
D_{max}	Maximum measured particle size in a given 10-sec sample
F	Parameter related to the gamma fitting function
g	Gravitational acceleration
IWC	Ice water content
k	Coefficient in equation for effective density
M	Moment number for fitting function
m	Ice particle mass
N	Concentration per unit diameter as a function of D (cm^{-4})
N_i	Concentration in probe size bin i
$N_0, N_{0\Gamma}$	Concentration intercept parameter, exponential, gamma distribution
N_t	Total concentration (cm^{-3}) of size distribution
n	Exponent in effective density relationship
P	Pressure (hPa)
PSD	Particle size distribution
p	Parameter giving the moment number for gamma fit
R	Precipitation rate ($mm\ hr^{-1}$
r_e	Radius used to describe the radiative properties of a particle population

r	Correlation coefficient
T	Temperature ($^{\circ}$C)
V_t, V_m, V_Z	Ice particle terminal velocity, mean mass-weighted, and mean reflectivity-weighted velocities of ice particle size spectra
y	Coefficient in mass versus diameter relationship
Z, dBZ_e	Radar reflectivity factor, equivalent radar reflectivity (db)
α	Exponent in effective density relationship
ϵ	Extinction coefficient
η	Exponent in mass versus diameter relationship
κ	Exponent in the terminal velocity versus diameter relationship
λ, λ_Γ	Slope parameter of size distribution for exponential, gamma PSDs
μ	Dispersion of gamma particle size distribution
ν	Kinematic viscosity
ρ_a	Air density
ρ_e	Effective ice particle density
ρ_i	Density of solid ice

Appendix B: Estimation of Ice Particle Mass and Terminal Velocity

The ice particle mass—a necessary input into calculations of the IWC, dBZ_e, and the mass-and reflectivity-weighted fall velocities (V_m and V_Z)—can be derived from Eq. (1). As no measurements of the IWC were obtained to provide constraints on the estimated ρ_e in Eq. (2), a comprehensive effort was undertaken to develop reliable estimates of ρ_e and hence m. This effort involved three independent approaches:

1. We compared calculations of the terminal velocities with observations of snow crystal V_t values at the ground, a meaningful test of the ρ_e relationship because $V_t \propto \rho_e^{0.4}$ to $\rho_e^{0.8}$.
2. We compared the comprehensive set of dBZ_e and V_Z values from the ARMAR (nadir viewing) on the DC-8 with calculations of these variables from the PSDs on the same days. The DC-8 generally avoided convection and measurements in convective cells that might have confounded this comparison.
3. We compared calculations of rain PSDs, using as input snow PSDs near the top of the melting layer, with measured rain PSDs at the base of the ML during spirals. This method proved inconclusive, because of continued particle growth in the larger sizes and depletion in the smaller sizes.

Our goal was to find a single relationship between ρ_e and D across the full range of observed particle sizes to simplify the development of parameterizations of the PSDs in terms of macroscale variables (e.g., IWC) as presented in section 5. Three techniques (shown in Table 4) satisfied this requirement. The one parameter approach ($\rho_e \propto$ D) (Table 4), employing the coefficients presented in Brown and Francis (1994) (hereafter BF94) which fit direct measurements of IWC and applied to ice clouds when particles were relatively dense and up to several millimeters in size., We also tested the two-parameter "area ratio" (A_r) approach, in which ρ_e is a function of D and A_r (H02) (hereafter H02). It is our belief—and supported by the observations by Hanesch (1999)—that there is inherent information on ρ_e in the A_r. The A_r two-parameter technique often reduces to a one parameter technique because A_r is usually approximately related to D by a power law. The two sets of coefficients shown for the A_r technique in Table 4 were developed for low ρ_e (A_r[I]), and for relatively high ρ_e associated with bullet rosettes up to about 0.1–0.2 cm (A_r[BR]). A third technique, a hybrid of the one-and two parameter techniques, was also attempted, as it captured the inherent information available in the two-parameter technique and the general decrease in ρ_e with D, which is commonly found in transitions from single crystals at small sizes to aggregates at large sizes. For the hybrid technique, we used two sets of coefficients, consistent with earlier observations of aggregates at the ground (designated as H[I] and H[II] in the table.

From the images of some of the particles shown in Figs. 8–10 as well as and others not shown, some inferences about the ρ_e may be made. Drawing upon observations in H01, the hexagonal plate and platelike crystals in the 400–600-μm range shown in Fig. 9. and larger than 800 μm in Fig. 15, have ρ_e values of 0.03–0.05 g cm^{-3}. The capped columns in Figs. 8–10 have $\rho_e \approx 0.15$ g cm^{-3}, and the columns in Fig. 10 have $\rho_e \approx 0.07$ g cm^{-3}. Inspection of the particles smaller than 100 μm indicate that they are not solid ice spheres. The ρ_e for the more complex, partially rimed crystal shapes cannot be ascertained from the images alone.

The ρ_e values as a function of D for the three techniques are plotted in Fig. 20A, using the coefficients given in Table 4. Using the second and third approaches, we derived A_r from $A_r = 0.4D^{-0.09}$, which represents an average relationship for the TRMM spirals. Use of the BF94 approach produced unrealistically large ρ_e values below about 500 μm and too small ρ_e values above 0.5 cm. Use of the A_r(I) technique resulted in intermediate ρ_e values at small sizes and relatively large ρ_e values at large sizes. The A_r(BR) technique, plotted over the applicable range of sizes, yielded relatively large ρ_e. Using the two sets of coefficients (I) and (II) for the hybrid approach shown in Table 4 produced comparable results, with relatively large ρ_e at small sizes and low ρ_e at large sizes.

The V_t was calculated as a function of D using the ρ_e from each approach. These calculated terminal velocities were then compared to a large set of V_t measurements for snowflakes that fell to the surface in Japan at T of $\approx$ —5°C (reported in Muramoto *et al.*, 1993) (Fig. 20B). The shaded region in the figure shows the $\pm$ 1σ bounds of the V_t observed in that study; are consistent with observations by many other We particularly plotted the data from the Muramoto study because these extend to somewhat smaller sizes. The V_t were calculated from Eq. (11).

The calculated V_t generally increased with D (Fig. 20B), with less of an increase above about 0.4 cm, marking a change in the a_f and b_f (drag-related) coefficients. The curve shown in the figure for BF95 data suggests that values in that study were ρ_e are overestimated for aggregates in the small sizes and underestimated in the large sizes. The V_t trends with D for the A_r technique suggest that the ρ_e values were are overestimated for D smaller than 0.05 cm using A_r(BR) and overestimated for D>0.5 cm for AR(I). The V_t trends with D for both hybrid approaches agreed well with the measured V_t for the larger sizes. The V_t below about 0.1 cm for the H(II) technique appear to be larger than observed for aggregates.

As a means of evaluating the estimates of m from Eqs. (1) and (2), we used the PSDs for all spirals and Eq. (1) to calculate the dBZ$_e$ ($\propto m^2$) and V_Z (related both to dBZ$_e$ and terminal velocity), then compared the results to the same parameters measured by

the ARMAR (nadir viewing) on the same days (Fig. 21). In the calculations of dBZ_e, 7.2 dB was subtracted from the reflectivities to account for the differences in the dielectric constants between water and ice. Note that there may be some residual mesoscale ascent of order 10 cm s^{-1} just above the ML in these plots that is not averaged out. The mean values from ARMAR were obtained above the ML during those periods when the DC-8 was in level flight and in most instances avoided convection. The four panels in the figure show the values calculated using the three techniques for obtaining ρ_e: the single parameter technique $\rho_e \propto D^b$; here b is a power (n = 0 in Eq. [2]); the A_r technique, $\rho_e = kA_r^n$ ($\alpha = 0$ in Eq. [2]); and the hybrid technique with two sets of coefficients. (The explicit equations used to derive ρ_e from the average TRMM A_r versus D relationship are given in Table 4.) Although the standard deviations of the V_Z are fairly large, a systematic increase of V_Z with dBZ is noted, but with some natural variability and some variability resulting from vertical motions.

Comparison of calculated and measured dBZ versus V_Z indicates that when the particles were small and the dBZ and V_Z were relatively low, the one-parameter technique, using the coefficients from BF95, produces results that overestimated V_Z; the A_r technique produced results that agreed moderately well with the radar data; and the hybrid (I) technique's calculations agreed well with the data for both sets of coefficients. When relatively large particles were present, at large dBZ and V_Z, the one-parameter technique significantly underpredicted the V_Z; the A_r(I) technique significantly overpredicted the V_Z; and the two hybrid approaches produced reasonable V_Z (I) and overpredicted the V_Z (II).

From these comparisons, we conclude that the hybrid (I) technique appears to give the most reasonable results.

REFERENCES

Brown, P.R.A., and P. N. Francis, 1994: Improved measurements of the ice water content in cirrus using a total-water probe. *J. Atmos. Oceanic Technol.*, **12**, 410–414.

Durden, S.L., E. Im, F.K. Li, W. Ricketts, A. Tanner, W. Wilson, 1994: ARMAR: An Airborne Rain-Mapping Radar. *J. Atmos. Oceanic Technol.*, **11**, 727-737.

Field, P. R., 1999: Aircraft observations of ice crystal evolution in an altostratus cloud. *J. Atmos. Sci.*, **56**, 1925-1941.

Fu, Q., 1996: An accurate parameterization of the solar radiative properties of cirrus clouds for climate models. *J. Cli.*, **9**, 2058-2082.

Gordon, G. L., and J. D. Marwitz, 1986: Hydrometeor Evolution in Rainbands over the California Valley. *J. Atmos. Sci.*, **43**, 1087–1100.

Griffith, K. T., S. K. Cox, and R. G. Knollenberg, 1980: Infrared radiative properties of tropical cirrus clouds inferred from aircraft measurements. *J. Atmos. Sci.*, **37**, 1077-1087.

Hanesch, M., 1999: Fall velocity and shape of snowflakes, Ph.D. thesis, Swiss Federal Institute of Technology, Zurich, Switzerland. Available from: http://e-collection.ethbib.ethz.ch/ediss/sg/070_e.html

Heymsfield, A. J., 1977: Precipitation development in stratiform ice clouds: A microphysical and dynamical study. *J. Atmos. Sci.*, **34**, 284–295.

_____, and J. L. Parrish, 1978: A computational technique for increasing the effective sampling volume of the PMS 2–D particle size spectrometer. *J. Appl. Meteor.*, **17**, 1566–1572.

_____, 1986: Ice particle evolution in the anvil of a severe thunderstorm during CCOPE. *J. Atmos. Sci.*, **43**, 2463–2478.

_____, and G. M. McFarquhar, 1996: On the high albedos of anvil cirrus in the tropical Pacific warm pool: Microphysical interpretations from CEPEX and from Kwajalein, Marshall Islands, *J. Atmos. Sci.*, *53*, 2401–2423.

_____, G.M. McFarquhar, W.D. Collins, J.A. Goldstein, F.P.J. Valero, J. Spinhirne, W. Hart, and P. Pilewskie, 1998: Cloud properties leading to highly reflective tropical cirrus: interpretations from CEPEX, TOGA COARE, and Kwajalein, Marshall Islands. *J. Geophys. Res.*, **103, D8**, 8805–8812.

_____, A. Bansemer, S. Lewis, J. Iaquinta, M. Kajikawa, C. Twohy, and M. R. Poellot, 2002: A general approach for deriving the properties of cirrus and stratiform ice cloud particles. *J. Atmos. Sci.*, in press.

_____, and L. M. Miloshevich, 2002: An explanation and parameterizations for the physical properties of cirrus and stratiform ice cloud particles. Part I: Cross-Sectional Area and Extinction. Submitted to *J. Atmos. Sci.*.

Heymsfield, G. M., S. W. Bidwell, I. J. Caylor, S. Ameen, S. Nicholson, W. Boncyk, L. Miller, D. Vandemark, P. E. Racette, and L. R. Dod, 1996: The EDOP Radar System on the High-Altitude NASA ER-2 Aircraft. *J. Atmos. Oceanic Technol.*, **4**, 795809.

Houze, R. A., P. V. Hobbs, P. H. Herzegh, and D. B. Parsons, 1979: Size Distributions of Precipitation Particles in Frontal Clouds. *J. Atmos. Sci.*, **36**, 156–162.

Knollenberg, R.G., A.J. Dascher, and D. Huffman, 1982: Measurements of the aerosol and ice crystal populations in tropical stratospheric cumulonimbus anvils. *Geophys. Res. Lett.*, **9**, 613-616.

Knollenberg, R. G., K. Kelly, and J. C. Wilson, 1993: Measurements of high number densities of ice crystals in the tops of tropical cumulonimbus, *J. Geophys. Res.*, *98*, 8639–8664.

Kosarev, A. L., and I. P. Mazin, 1991: An empirical model of the physical structure of upper layer clouds. *Atmos. Res.*, **26**, 213–228.

Kozu, Toshiaki, Kenji Nakamura, 1991: Rainfall Parameter Estimation from Dual-Radar Measurements Combining Reflectivity Profile and Path-integrated Attenuation. *J. Atmos. Ocean. Tech.*, **8**, 259270.

Lo, K. Kenneth, and R. E. Passarelli, Jr., 1982: Growth of snow in winter storms; an airborne observational study. *J. Atmos. Sci.*, **39**, 697–706.

McFarquhar, G. M., and A. J. Heymsfield, 1996: Microphysical characteristics of three cirrus anvils sampled during the Central Equatorial Pacific Experiment, *J. Atmos. Sci.*, *53*, 2401–2423.

McFarquhar, G.M., and A.J. Heymsfield, 1997: Parameterization of tropical cirrus ice crystal size distributions and implications for radiative transfer: results from CEPEX. *J. Atmos. Sci.*, **54**, 2187-2200.

Mitchell, D. L., 1991: Evolution of snow-size spectra in cyclonic storms. Part II: Deviations from the exponential form. *J. Atmos. Sci.*, **48**, 1885-1899.

Mitchell, D. L., 1996: Use of mass- and area-dimensional power laws for determining precipitation particle terminal velocities. *J. Atmos. Sci.*, **53**, 1710–1723.

Muramoto, K-I., K. Matsura, T. Harimaya, and T. Endoh, 1993: A computer database for falling snowflakes. *Ann. Glac.*, **18**, 11–16.

Passarelli, Richard E., Jr., 1978: Evolution of snow size spectra in winter storms. Cloud Physics Lab., Technical Note 52, Dept. of Geophysical Sciences, Univ. of Chicago, M.G.A. (1978), 29:6-391, 100 pgs.

Pueschel, R. F., D. A. Allen, C. Black, S Faisant, G. V. Ferry, S. D. Howard, J. M. Livingston, J. Redemann, C. E. Sorenson and S. Verma, 1995: Condensed water in tropical cyclone "Oliver", 8 February 1993. *Atmos. Res.*, **38**, *38*, 297–313.

Rossow, W. B., R. A. Schiffer, 1999: Advances in Understanding Clouds from ISCCP. *Bull. Amer. Meteor. Soc.*, , **80**, 22612288.

Ryan, B. F., 2000: A bulk parameterization of the ice particle size distribution and the optical properties in ice clouds. *J. Atmos. Sci.*, **51**, 1436–1451.

Schumacher, C., and R. A. Houze, Jr., 2001: Comparison of Radar Data from the TRMM Satellite and Kwajalein Oceanic Validation Site. *J. Appl. Meteor.*, **39**, 2151–2164.

Sekhon, R. S., and R.C. Srivastava, 1970: Snow Size Spectra and Radar Reflectivity. *J. Atmos. Sci.*, , **27**, 299–307.

Smith, P. L., 1984: Equivalent radar reflectivity factors for snow and ice particles. *J. Appl. Meteor.*, **23**, 1258–1260.

Stith, J. L., J. E. Dye, A. Bansemer, A. J. Heymsfield, C. A. Grainger, W. A. Petersen and R. Cifelli, 2002; Microphysical Observations of Tropical Clouds. *J. Appl. Meteor.*, in press.

Takahashi, T., and K. Kuhara, 1993: Precipitation mechanisms of cumulonimbus clouds. *J. Met. Soc. Japan*, **71**, 21–31.

Willis, P. T., and A. J. Heymsfield, 1989: Structure of the melting layer in mesoscale convective storm stratiform precipitation. *J. Atmos. Sci.*, **46**, 2008-2025.

Yokoyama, T., 1985: Observation of microphysical processes in the stratiform precipitations including melting layers at Mt. Fuji. *J. Met. Soc. Japan*, **63**, 100–111.

Zhang, G., J. Vivekanandan, and E. Brandes, 2001: A method for estimating rain rate and drop size distribution from polarimetric radar measurements. *IEEE Transact. Geosci. Remote Sens.*, **39**, 830–841.

Table 1

INSTRUMENTS USED IN EARLIER TROPICAL ICE CLOUD STUDIES

Study	Probe	Range (μm)	Probe	Range (μm)	Probe	Range (μm)
Griffith et al. (1980)	1D-C PMS[1] probe	70—460				
Knollenberg et al. (1982)	2D grey	40—2500				
Knollenberg et al. (1993)	FSSP[2]	0.1–78	2D grey	50—1500		
Takahashi and Kuhara (1993)	videosonde	200–$>$ 2000				
Pueschel et al. (1995)	2D grey	25–1800				
Heymsfield and McFarquhar (1996) McFarquhar and Heymsfield (1996) McFarquhar and Heymsfield (1997)	FSSP	0.1–21	VIPS[3]	10–200	2D—C	40–1000
Stith et al. (2001)	FSSP	2–45 μm	2D—C	40–1000	CPI[4]	$<$2 mm

[1] Particle Measuring Systems

[2] forward scattering spectrometer probe

[3] video ice particle sampler

[4] cloud particle imager

Table 2

TRMM Lagrangian Spiral Descents

Date	Location	Times (UTC)	Alt (m)	Temp (° C)	$\overline{\frac{d(Alt)}{dt}}$ (m s^{-1})	Loops (#)	Op. Depth (Average)	Radar Sfc. Precip (Any–>18 dBZ)	Radar Change (dB)
980905	Fla[1]	213251 215040	7923 3632	-19 6	2.7	6	N/A	Yes Yes	$< \pm 5$
990217	Brazil	194224 195601	10042 4602	-38 0	6.7	4	N/A	Yes Yes	$< \pm 5$
990219	Brazil[2]	201335 201934	6091 4379	-10 2	4.8	3	N/A	Yes Yes	≈ 10
990818	Kwajalein	035139 040701	8508 5695	-26 -5	3.1	7	24	Yes No	$+5$
990819	Kwajalein	220448 225000	6950 3370	-14 7	1.3	23	37	Yes Early	-25
990822	Kwajalein	212049 220451	11206 6983	-50 -16	1.6	14	22	No No	Not detect.
990823	Kwajalein,	031450 034550	10341 6094	-42 -9	2.3	10	25	Yes Yes	$< \pm 5$
990830	Kwajalein	201056 203730	7376 3685	-18 6	2.3	13	29	Yes Yes	-10
		205332 212120	7319 3685	-17 5	2.2	13	25	Yes Yes	-25
990911	Kwajalein	194955 203121	10055 4514	-39 7	2.2	11	30	Yes Yes	-20

[1] Near Cape Kennedy [2] Near Puerto Velho N/A–Not available or unknown

Table 3

Equations to Derive $N_{0\Gamma}$, λ_Γ from Microphysical and Radar Variables

Variable	Full Equation	Simplified Equation
IWC $[\frac{g}{m^3}]$	$\frac{N_{0\Gamma}\pi k a^n \text{x}10^6\Gamma(4+bn+\alpha+\mu)}{6\lambda_\Gamma{}^{(4+bn+\alpha+\mu)}}$	$\frac{3.3 \text{ x } 10^3 N_{0\Gamma}\Gamma(3.2+\mu)}{\lambda_\Gamma{}^{(3.2+\mu)}}$
$\mathbf{D}_{mm}$ [cm]	$\frac{3 + \alpha + bn + \mu + 0.67}{\lambda_\Gamma}$	$\frac{2.90 + \mu}{\lambda_\Gamma}$
Z $[\frac{mm^6}{m^3}]$	$\frac{N_{0\Gamma}k^2 a^{2n}\text{x}10^{12}\Gamma(7+2(bn+\alpha)+\mu)}{{\rho_w}^2\lambda_\Gamma{}^{(7+2(bn+\alpha)+\mu)}}$	$\frac{3.90 N_{0\Gamma} \text{ x } 10^7\Gamma(5.5+\mu)}{\lambda_\Gamma{}^{(5.5+\mu)}}$
dBZ_e[1]	$10 \log_{10}Z - 7.2$	$10 \log_{10}Z - 7.2$
$\mathbf{V}_m$ $[\frac{cm}{s}]$	$\frac{C\lambda_\Gamma{}^{(-\kappa)}\Gamma(\kappa+4+bn+\alpha+\mu)}{\Gamma(4+bn+\alpha+\mu)}$	$\frac{274\Gamma(3.8+\mu)\lambda_\Gamma{}^{-0.53}}{\Gamma(3.8+\mu)}$
V_Z $[\frac{cm}{s}]$	$\frac{C\lambda_\Gamma{}^{(-\kappa)}\Gamma(\kappa+7+2(bn+\alpha)+\mu)}{\Gamma(7+2(bn+\alpha)+\mu)}$	$\frac{218\Gamma(5.6+\mu)\lambda_\Gamma{}^{-0.12}}{\Gamma(5.5+\mu)}$
R $[\frac{mm}{hr}]$	$\frac{0.036 N_{0\Gamma}\pi k a^n C\text{x}10^6\Gamma(\kappa+4+bn+\alpha+\mu)}{6\lambda_\Gamma{}^{(\kappa+4+bn+\alpha+\mu)}}$	$\frac{3.2 \text{ x } 10^4 N_{0\Gamma}\Gamma(3.8+\mu)}{\lambda_\Gamma{}^{(3.8+\mu)}}$
A_c $[\frac{cm^2}{m^3}]$	$\frac{N_{0\Gamma}\pi a \text{x}10^6\Gamma(3+b+\mu)}{4\lambda_\Gamma{}^{(3+b+\mu)}}$	$\frac{2.3\text{x}10^5 N_{0\Gamma}\Gamma(2.8+\mu)}{\lambda_\Gamma{}^{(2.8+\mu)}}$
ϵ $[km^{-1}]$	$0.2A_c$	$0.2A_c$
r_e $[\mu m]$	$\frac{2\sqrt{(3)}k a^{n-1}\text{x}10^4\Gamma(4+bn+\alpha+\mu)}{9\rho_i\Gamma(3+b+\mu)\lambda_\Gamma{}^{(1+b(n-1)+\alpha)}}$	$\frac{91\Gamma(3.2+\mu)}{\Gamma(2.8+\mu)\lambda_\Gamma{}^{0.41}}$

[1] Assumes Rayleigh scatters, valid for radar wavelengths of 2.1 cm and above. **Units unless otherwise stated: cgs.**

Equations based on the following relationships:

Mass: $m = \frac{\pi}{6}\rho_e D^3$.

Effective density: $\rho_e = k(A_r)^n D^\alpha$, k = 0.04, n = 1.5, α = -0.5

Area Ratio TRMM average values: a = 0.29, b = -0.18.

Terminal Velocity: $V_t = a_f(\frac{4gka^{n-1}}{3\rho_a})^{b_f}\nu^{(1\ -\ 2b_f)}D^{[(3+b(n-1)+\alpha)b_f-1]}$,

Drag Coefficient Parameters: For V_m and R, a_f = 0.2072, b_f = 0.638, for V_Z, a_f = 1.0865, b_f = 0.499.

Kinematic viscosity: ν, **Air density:** ρ_a

Simplified equations for P = 500 hPa, T = 0°C

$\kappa = (3 + b(n-1) + \alpha)b_f - 1$

$C = a_f[\frac{4gk}{3\rho_a}]^{b_f}\nu^{(1-2b_f)}a^{(n-1)b_f}$

Fitted Functions

Fitted Parameters	Fit to Median	Fit to median -1σ values	Fit to median +1σ values
λ_Γ vs T(°C)	$\lambda_\Gamma = 6.8\exp^{(-0.096T)}$	$4.0\exp^{(-0.10T)}$	$11.5\exp^{(-0.093T)}$
<-27C	$\lambda_\Gamma = 24.0\exp^{(-0.049T)}$	$10.8\exp^{(-0.063T)}$	$53.3\exp^{(-0.034T)}$
λ vs T	$\lambda = 12.5\exp^{(-0.066T)}$	$9.3\exp^{(-0.063T)}$	$16.7\exp^{(-0.069T)}$
μ vs N_0	$\mu = 0.21 \ln(0.12N_{0\Gamma})$	$\mu = 0.21 \ln(0.04N_{0\Gamma})$	$\mu = 0.21 \ln(0.33N_{0\Gamma})$
μ vs λ_Γ	$\mu = 0.13\lambda_\Gamma{}^{(0.64)} - 2$	$\mu = 0.14\lambda_\Gamma{}^{(0.59)} - 2$	$\mu = 0.11\lambda_\Gamma{}^{(0.72)} - 2$
Area Ratio=aD^b			
	a =$0.32\lambda_\Gamma{}^{-0.048}$	$0.31\lambda_\Gamma{}^{-0.062}$	$0.33\lambda_\Gamma{}^{-0.036}$
	b =-0.45+0.90a	-0.42+0.75a	-0.47+1.04a
Maximum Diam.			
	D_{max}=$9.5\lambda^{-0.91}$	$8.3\lambda^{-0.84}$	$10.4\lambda^{-0.98}$
	D_{max}=$3.2\lambda_\Gamma{}^{-0.61}$	$3.4\lambda_\Gamma{}^{-0.56}$	$3.1\lambda_\Gamma{}^{-0.64}$

Incomplete gamma function: $\gamma(a,x) = \int_0^x t^{(a-1)} e^{-t} dt.$

Example: $IWC = \frac{N_{0\Gamma} \pi k a^n \gamma(4 + bn + \alpha + \mu, \lambda_\Gamma D_{max})}{6 \lambda_\Gamma^{(4 + bn + \alpha + \mu)}}$

Table 4

Parameters Used to Calculate ρ_e

Technique	Equation	Designation	Coefficients	→	Simplified Eqn.
One–Parameter	$\rho_e = aD^b$		a = .00561	b = -1.1	
Two–Parameter	$\rho_e = k(A_r)^n$				
		A_r(I)	k = 0.18	n = 2.50	$\rho_e = 0.0182D^{-0.225}$
		A_r(BR)	k = 0.48	n = 2.25	$\rho_e = 0.0611D^{-0.203}$
Hybrid	$\rho_e = k(A_r)^n D^\alpha$				
		H(I)	k = 0.03	n = 1.2	$\rho_e = 0.0067D^{-0.508}$
			α = -0.4		
		H(II)	k = 0.04	n = 1.5	$\rho_e = 0.010D^{-0.635}$
			α = -0.5		

See Appendix B for discussion of nomenclature

Figure Captions

Figure 1. Flight tracks of DC-8 and Citation during Lagrangian spiral descent on 0819 (top) and 0823 (bottom), both from KWAJEX. Period of DC-8 overpass of Citation track is shown with bold line.

Figure 2. Radar data as a function of height from ARMAR (top five rows) and EDOP (bottom two rows) averaged over time periods when DC-8 or ER-2 crossed over or in proximity to Citation track. Radars are nadir viewing and times are indicated in left panels.Left: Mean measured dBZ$_e$, with $\pm 1\ \sigma$ bounds over periods shown. Right panels: Doppler velocity, and $\pm 1\sigma$ bounds of measured V_Z over periods are shown.

Figure 3. Average PSDs for various loops of the 990819 spiral. Heavy lines: 2D-C. Light lines: HVPS.

Figure 4. Measured reflectivities (left) and representations of the PSDs (right) during Lagrangian spiral descents on three days during KWAJEX. ARMAR measurements were obtained from DC-8 in nadir-viewing mode, with abscissa showing time. The boxes (left panels) show the top, bottom, and approximate horizontal positions of the Citation as if the spiral occurred during the overpass period (see text).

Figure 5. Same as Fig. 4, except that bottom panels shows data from EDOP on the ER-2 (data courtesy of Gerry Heymsfield) during LBA. Data for 990830 is from the first spiral listed in Table 2.

Figure 6. Examples of particles imaged by the HVPS probe for the 14 loops (numbered in panels) of the spiral on 990822. The scale is shown in the top left panel.

Figure 7. Concentration of particles 100 μ and above as measured by the 2D-C probe during five of the Lagrangian spiral descents. The distinct spikes at some points in the N_T traces in the ML are probably an artifact of the 2D-C probe.

Figure 8. Examples of particles imaged in three size ranges by CPI probe on 990819. Magnification between different size ranges is not the same.

Figure 9. Same as Fig. 8, except for 990822 (KWAJEX).

Figure 10. Same as Fig. 8, except for 990217 (LBA, top) and 0823 (KWAJEX, bottom). The 990217 case shows riming near to convection and the 990823 case shows pristine cirrus-type crystals reflecting short-lived convective elements and low temperatures

Figure 11. Microphysical variables derived from PSDs for three spirals. Rows from top to bottom: IWC, R, dBZ$_e$ as calculated assuming equivalent water spheres, V_Z, and V_m.

Figure 12. Fit parameters for exponential (left) and gamma (right) distributions as functions of T from 1–km PSDs. Top panels: λ and λ_Γ. Fit from Ryan (1996) and to the TRMM data in left panel, and to TRMM data in right panel, shown with solid line. Fits exclude 0822 case. Middle panels: N_0 and $N_{0\Gamma}$. Bottom left:

correlation coefficient. Bottom right: μ versus T. Different colors represent different days. Inserts in panels B, C, D: data for 0911 case.

Figure 13. Findings from the gamma distribution fits. A: Exponential versus gamma λ values. Solid line, 1:1 line; dashed: Fit. B: λ_Γ calculated from T versus measured. C, D: μ versus λ_Γ, μ versus $N_{0\Gamma}$. Mean and $\pm$ 1σ bounds in equal intervals of abscissa variable. Fits to the data (excluding 0822 case).

Figure 14. Maximum particle diameter per 1 km (about 8–9 sec) PSD as a function of λ (top) and λ_Γ (bottom).

Figure 15. N_0 versus λ (top) and $N_{0\Gamma}$ versus λ_Γ for the various spirals. Large symbols represent data points at 0 and 3°C.

Figure 16. Coefficients in the relationship $A_r = aD^b$ as derived by fitting the A_r versus D data from the imaging probes. A, B: Height dependence. C, D: Temperature dependence. E: Dependence of a on λ. F: Relationship between a and b coefficients.

Figure 17. Ratios of various parameters as obtained from the fitted size distributions to those calculated from the PSDs.

Figure 18. The N_0 versus λ points measured during Lagrangian spirals by Gordon and Marwitz (1986), Lo and Passarelli (1982), Passarelli (1978), and Field (1999). Unless otherwise noted, data are from descents. The listed values in GM86 (2D-C probe) and the values extracted from the graphical plots in P78 and LP82 (1D-P probe) are plotted. Temperatures at top and bottom of each spiral are shown. The dotted lines show IWCs calculated using the Brown and Francis (1995) ρ_e–D relationship. The dashed lines in the lower right panel show an envelope of the observations from TRMM. The lines labeled "Ryan" use the λ–T relationship from Eq. (8) to predict λ from T, plotted at the measured value of N_0.

Figure 19. Comparison of the Sekhon and Srivastava (1970) parameterizaton (solid line) with the TRMM results (points). The line was obtained by the method described in section 5, with the squares along the line corresponding to the four precipitation rates that were used to develop the parameterization. The unmelted $N_0 - -\lambda$ points and the "melted equivalent" points were obtained from the 990822 spiral descent.

Figure 20. Top: The ρ_e usingthe one–and two–parameter techniques as well as the hybrid technique. Bottom: Corresponding V_t, compared with data from Muramoto et al. (1993), shaded region.

Figure 21. Comparison of measured V_Z–dBZ$_e$ from ARMAR radar (mean and $\pm$1 σ bounds) with values calculated from PSDs (assuming equivalent water spheres) using (A) one–parameter technique with Brown and Francis (1995) coefficients, (B) A$_r$ technique, (C) H(I) technique, and (D) H(II) technique (coefficients listed in Table 4).

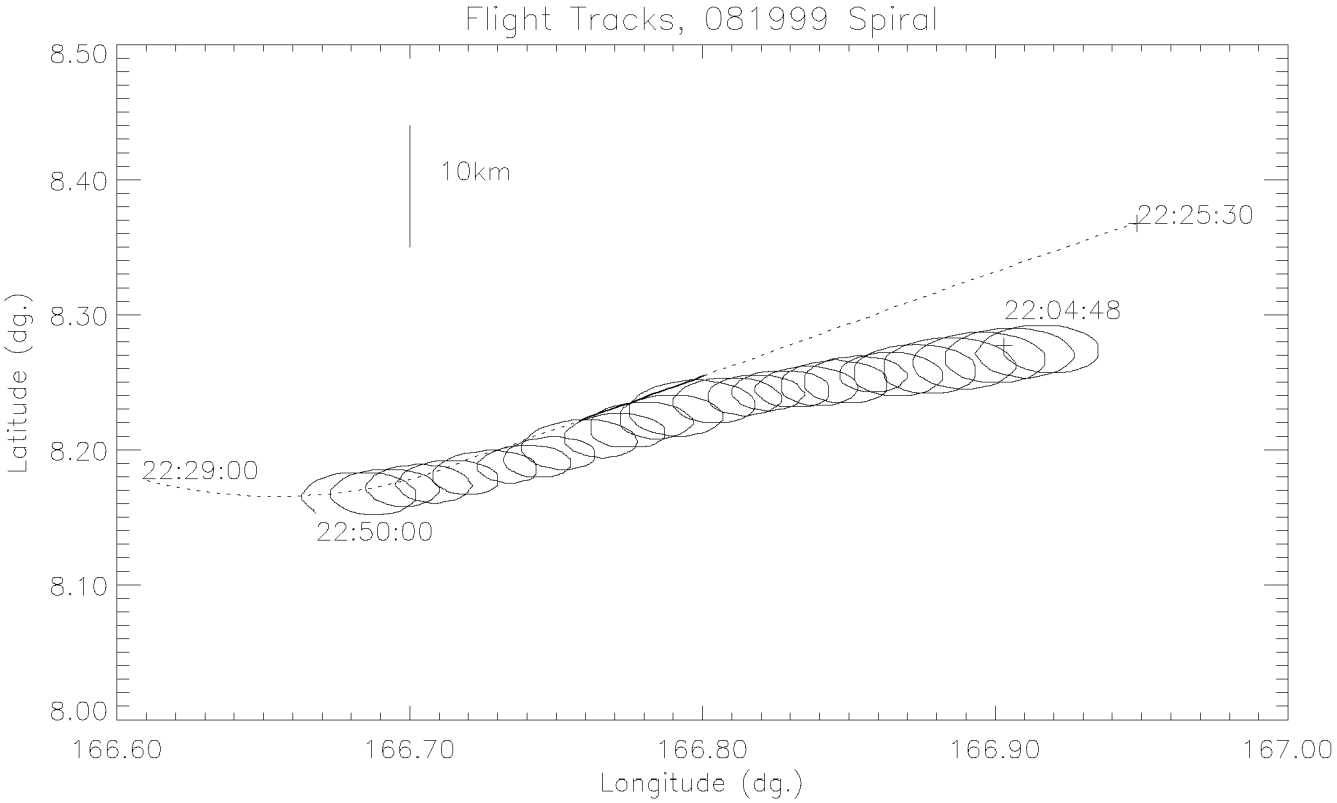
Flight Tracks, 081999 Spiral
8.50
8.40
8.30
8.20
8.10
8.00
Latitude (dg.)
10km
22:25:30
22:04:48
22:29:00
22:50:00
166.60
166.70
166.80
166.90
167.00
Longitude (dg.)

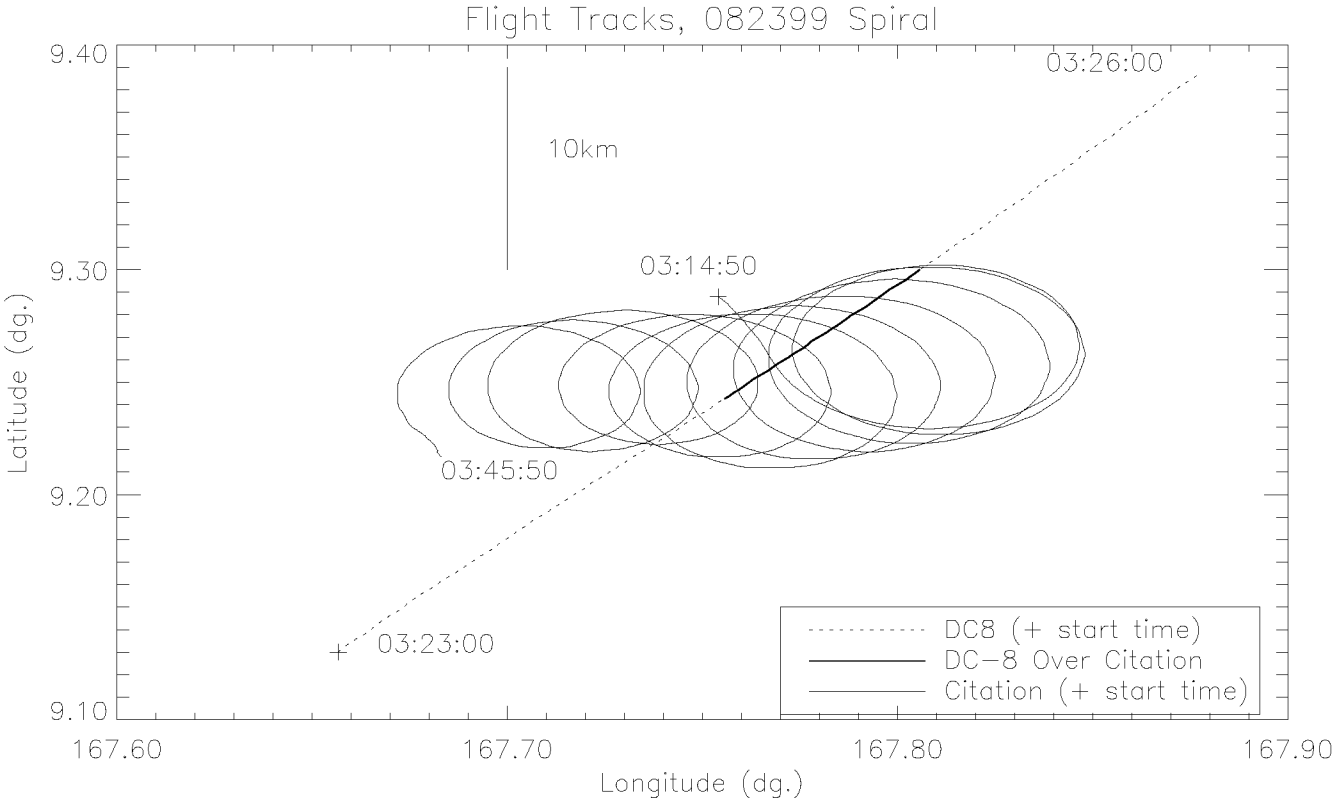
Flight Tracks, 082399 Spiral
9.40
9.30
9.20
9.10
Latitude (dg.)
03:26:00
10km
03:14:50
03:45:50
03:23:00
DC8 (+ start time)
DC-8 Over Citation
Citation (+ start time)
167.60
167.70
167.80
167.90
Longitude (dg.)

Reflectivity Doppler Velocity

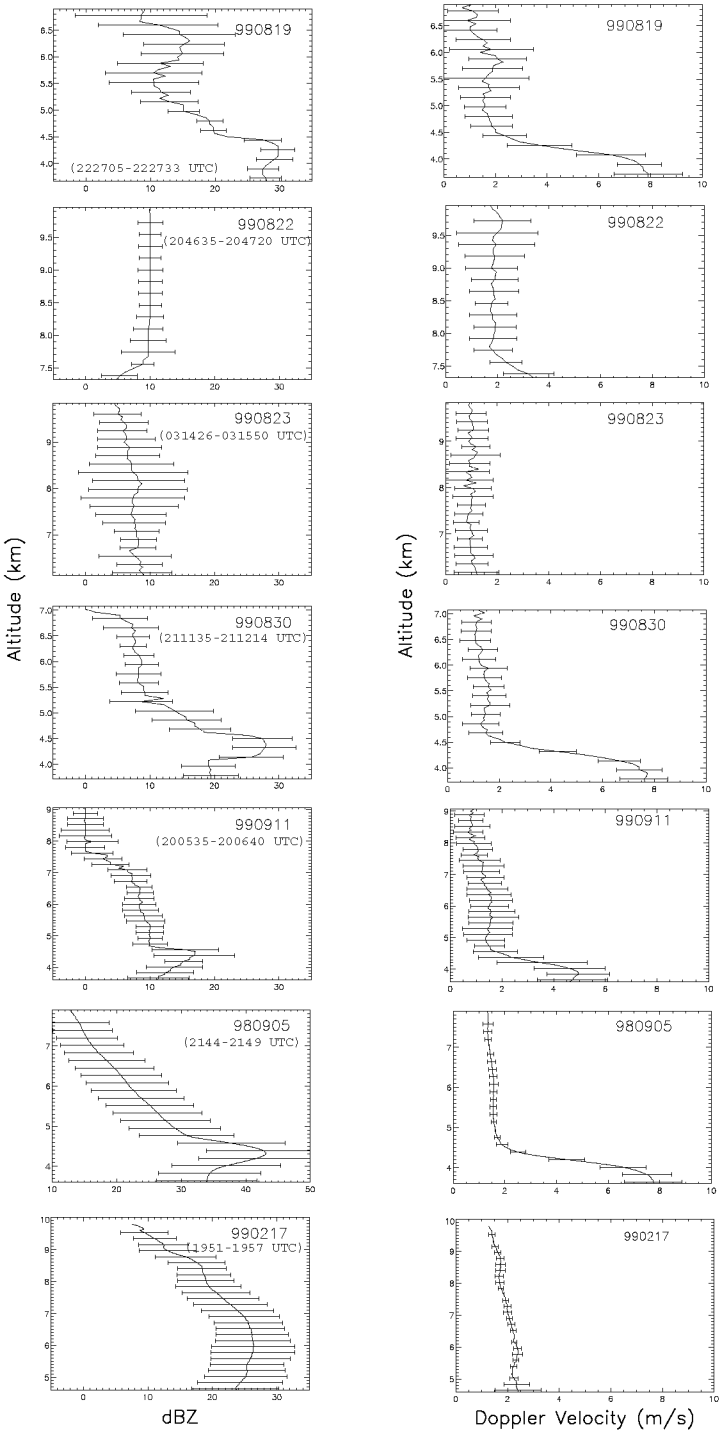

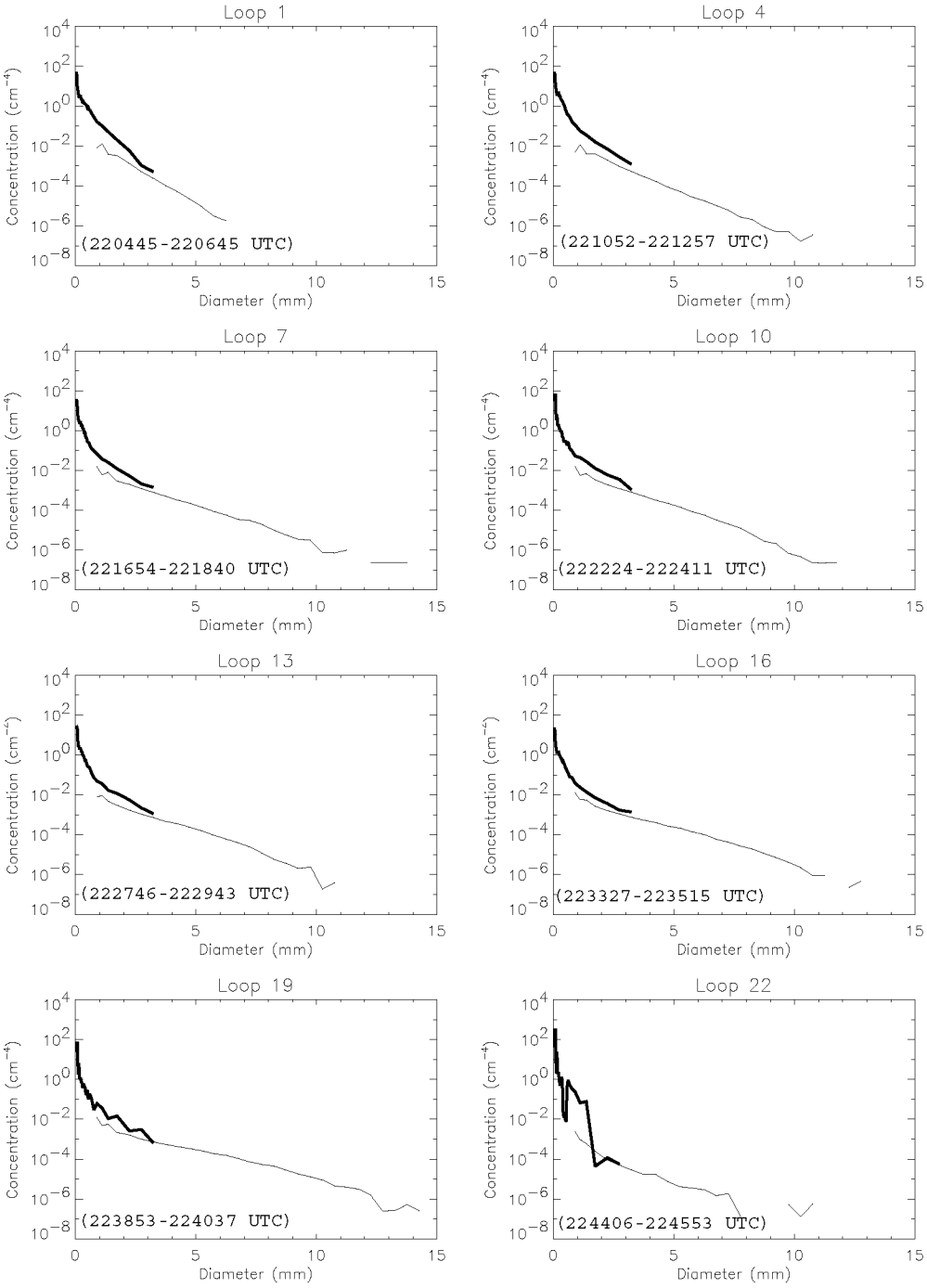
Loop 1
(220445-220645 UTC)
Loop 4
(221052-221257 UTC)
Loop 7
(221654-221840 UTC)
Loop 10
(222224-222411 UTC)
Loop 13
(222746-222943 UTC)
Loop 16
(223327-223515 UTC)
Loop 19
(223853-224037 UTC)
Loop 22
(224406-224553 UTC)
Concentration (cm^{-4})
Diameter (mm)

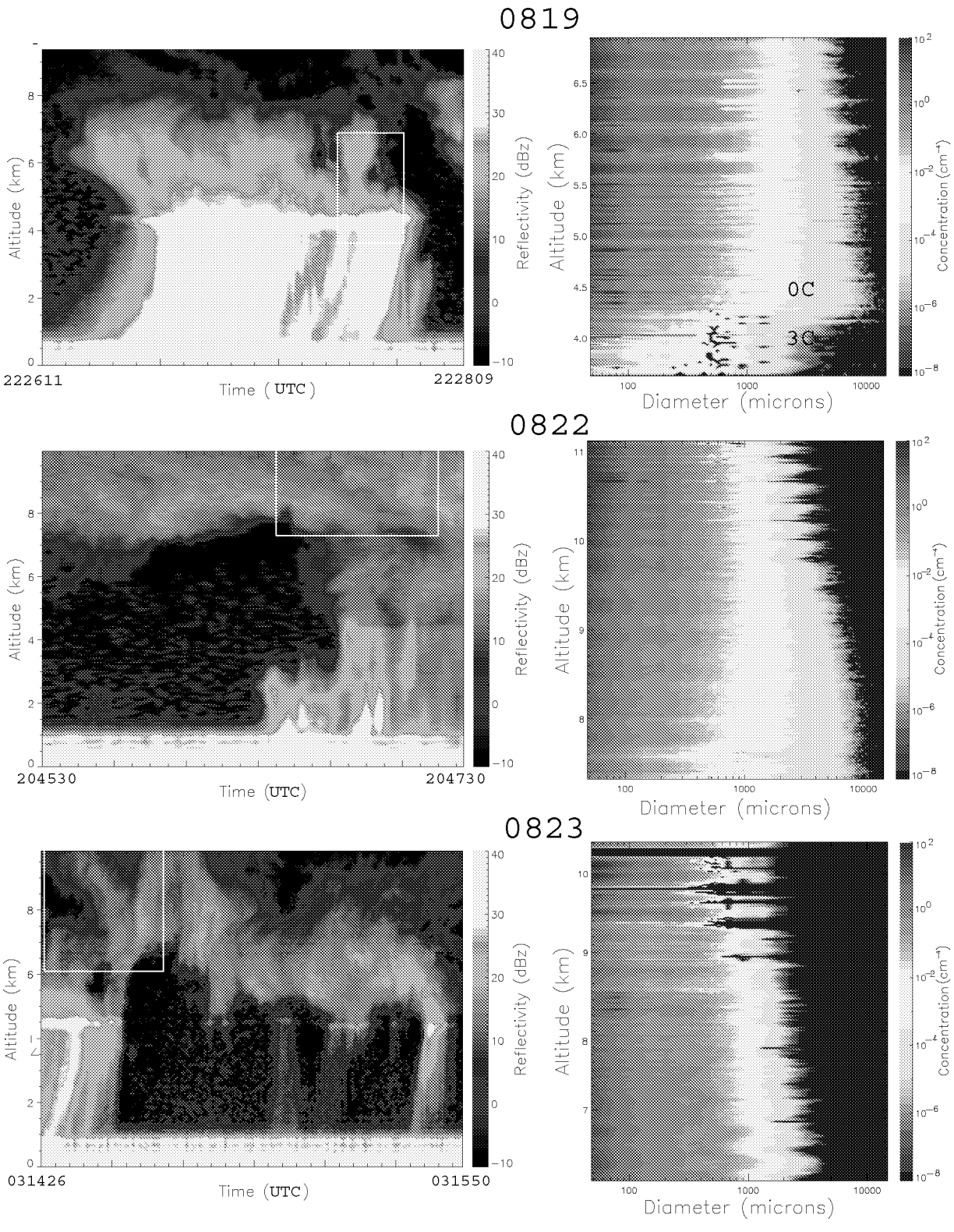
0819
Altitude (km)
Reflectivity (dBz)
222611
222809
Time (UTC)
Altitude (km)
0C
3C
Concentration (cm⁻⁴)
Diameter (microns)
0822
Altitude (km)
Reflectivity (dBz)
204530
204730
Time (UTC)
Altitude (km)
Concentration (cm⁻⁴)
Diameter (microns)
0823
Altitude (km)
Reflectivity (dBz)
031426
031550
Time (UTC)
Altitude (km)
Concentration (cm⁻⁴)
Diameter (microns)

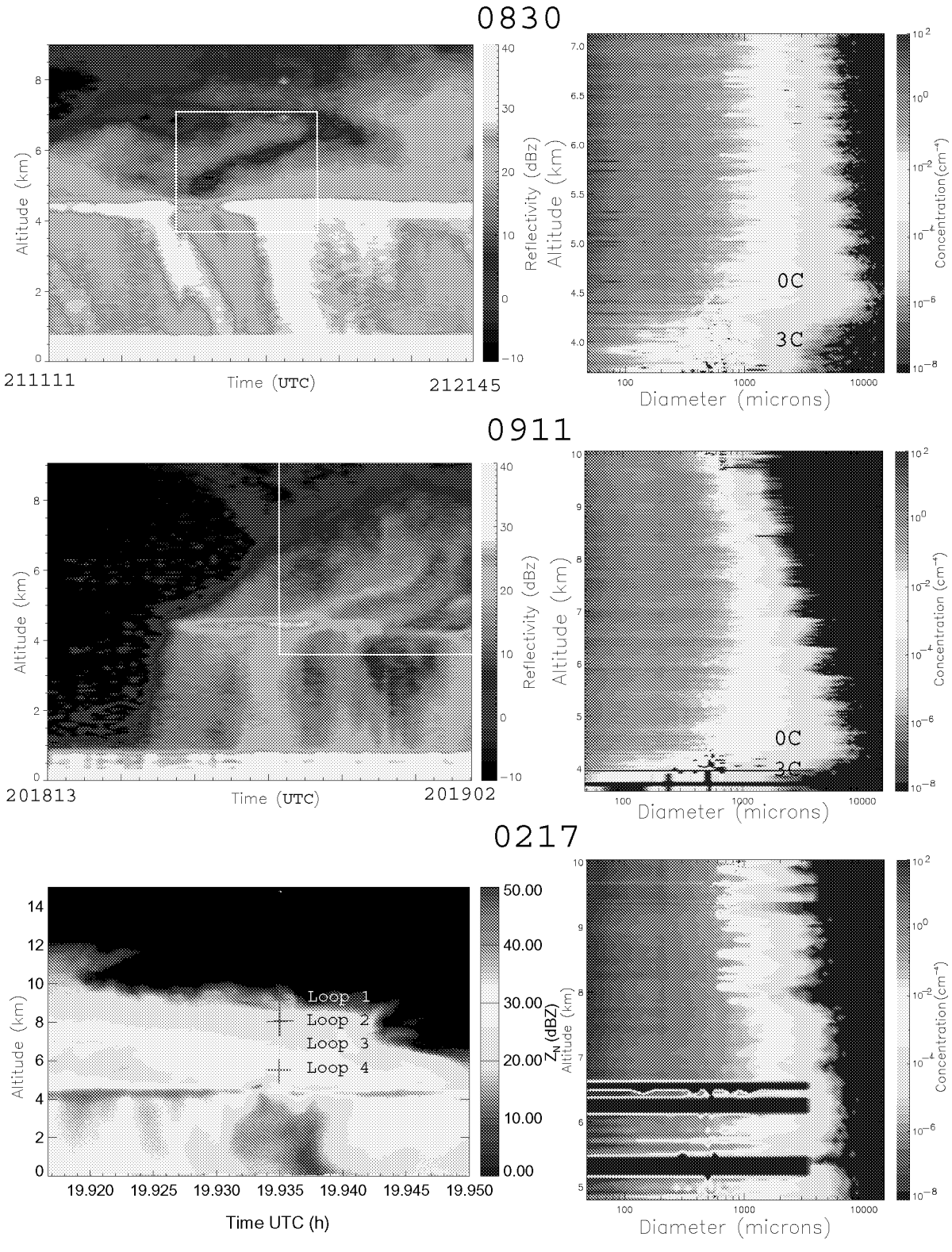
0830
Altitude (km)
Time (UTC)
211111
212145
Reflectivity (dBz)
Altitude (km)
0C
3C
Diameter (microns)
Concentration(cm⁻⁴)
0911
Altitude (km)
Time (UTC)
201813
201902
Reflectivity (dBz)
Altitude (km)
0C
3C
Diameter (microns)
Concentration (cm⁻⁴)
0217
Loop 1
Loop 2
Loop 3
Loop 4
Altitude (km)
Time UTC (h)
Z_N (dBZ)
Altitude (km)
Diameter (microns)
Concentration(cm⁻⁴)

990822
HVPS

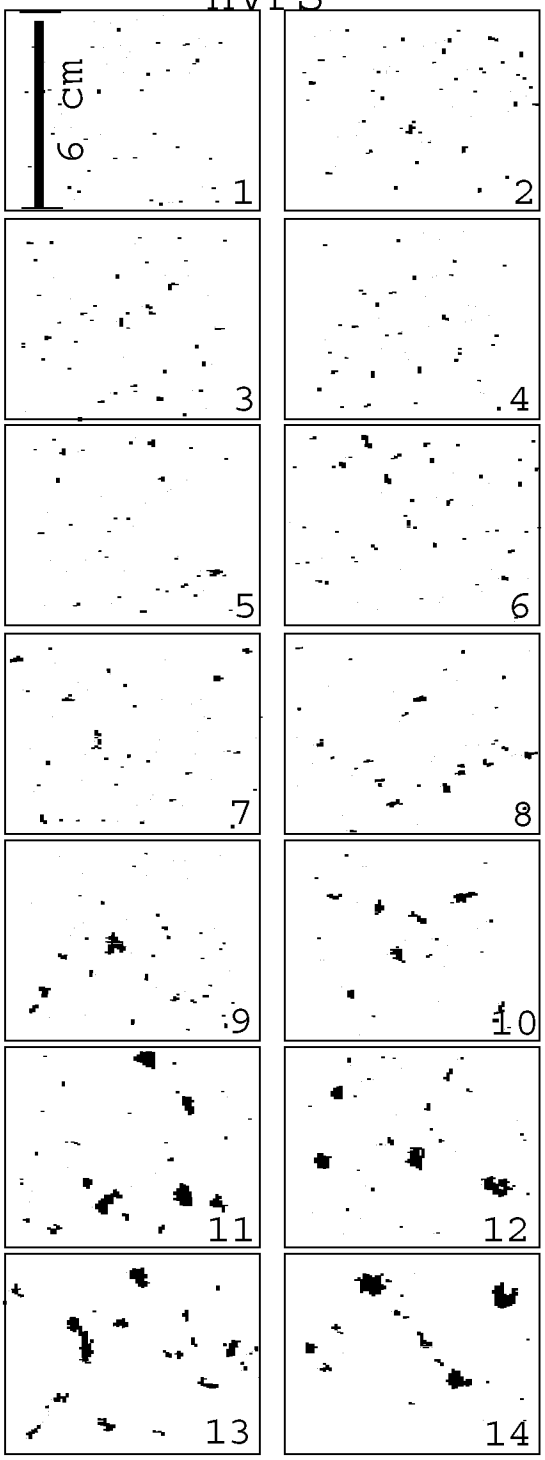

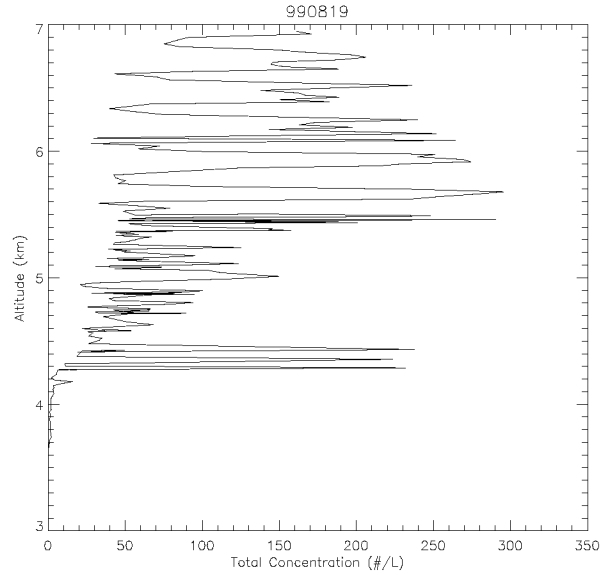
990819
Altitude (km)
Total Concentration (#/L)

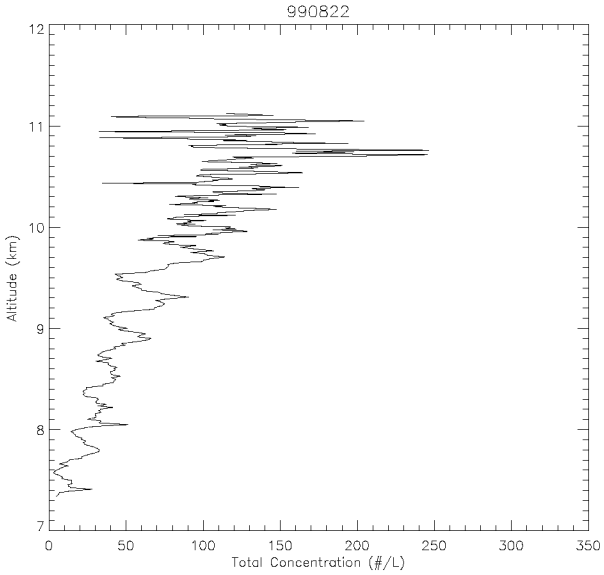
990822
Altitude (km)
Total Concentration (#/L)

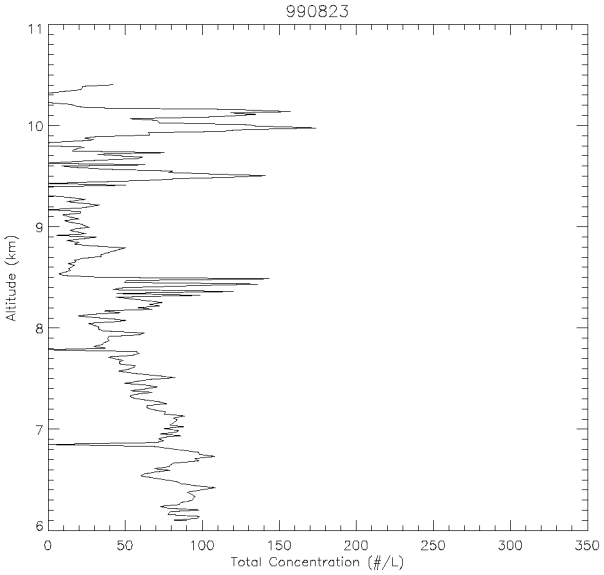
990823
Altitude (km)
Total Concentration (#/L)

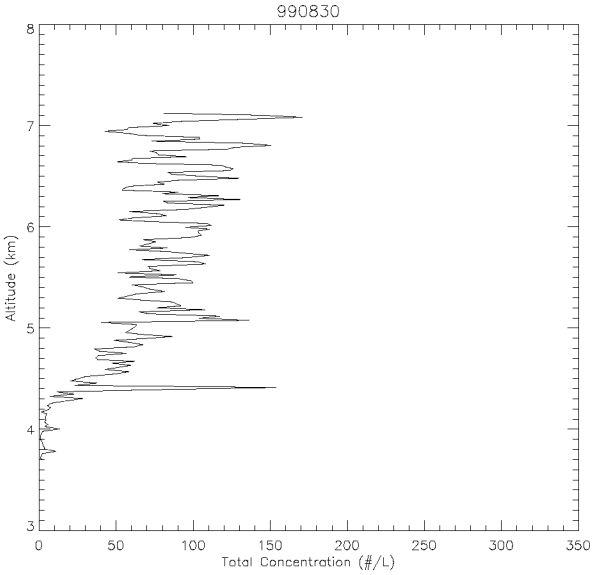
990830
Altitude (km)
Total Concentration (#/L)

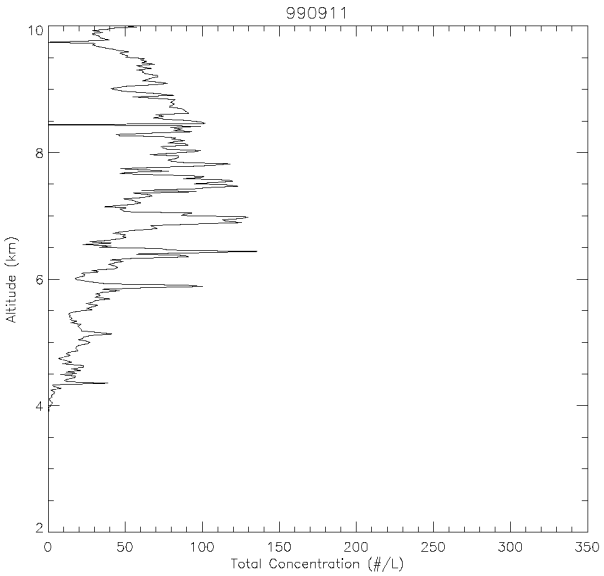
990911
Altitude (km)
Total Concentration (#/L)

Diameter (μm)
<100
400-600
>800
7.0
6.5
6.0
5.5
5.0
4.5
-15
-10
0
2
Altitude (km)
Temperature (C)
100μm
600μm
1000μm

D <100μm
400 to 600μm
>800μm
Height (km)
11.5
11
10.5
10
9.5
9
8.5
8
7.5
-50
-40
-30
-20
Temperature (C)
100μm
600μm
1000μm

Altitude (km)
Temperature (C)
<100
400-600
>800
10km
9km
-37
-30
-21
100μm
600μm
1000μm
<100
400-600
>800
-27
-20
-12
100μm
600μm
1000μm

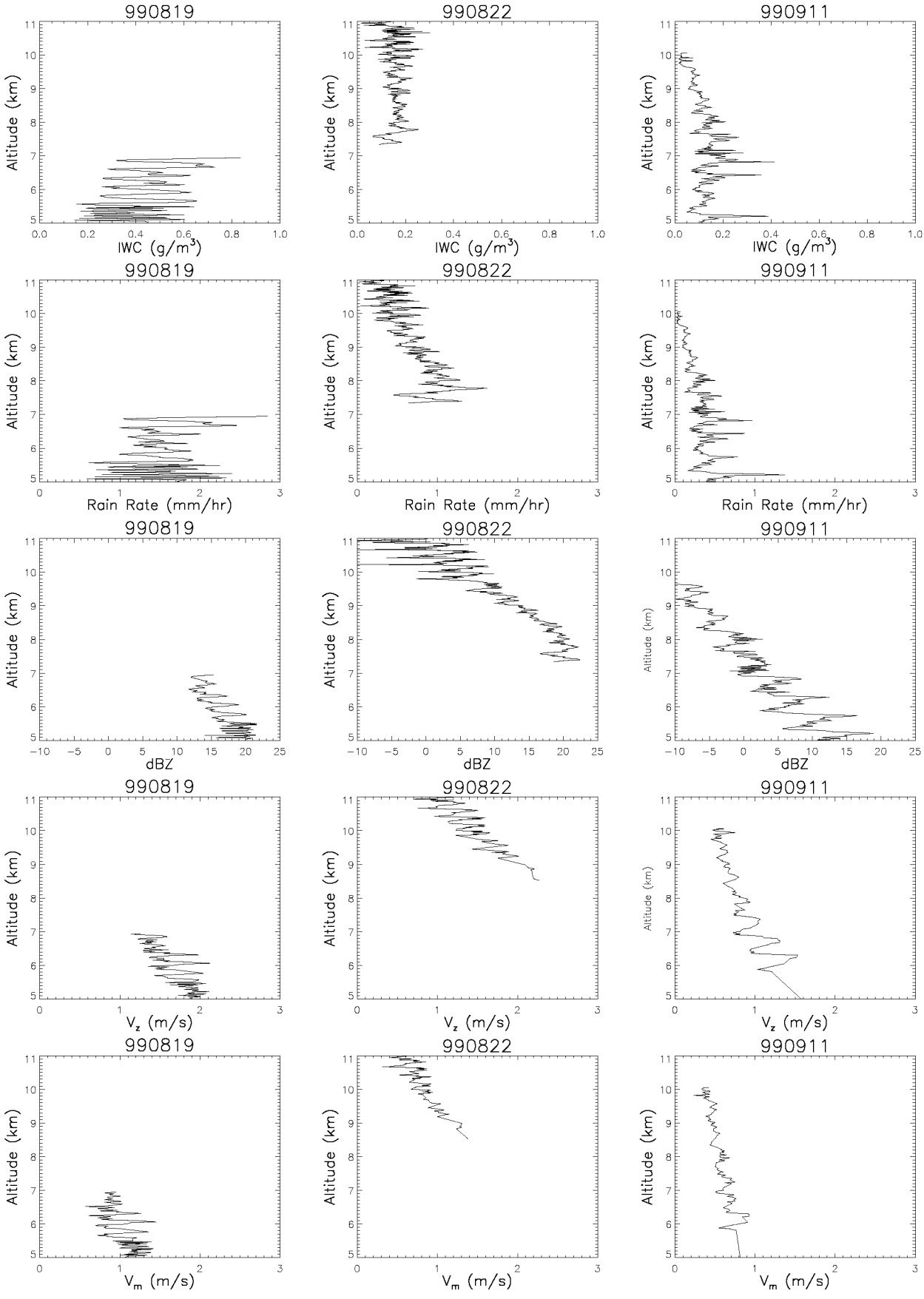
990819
990822
990911
Altitude (km)
IWC (g/m3)
Rain Rate (mm/hr)
dBZ
Vz (m/s)
Vm (m/s)

Spectral Parameters vs. Temperature

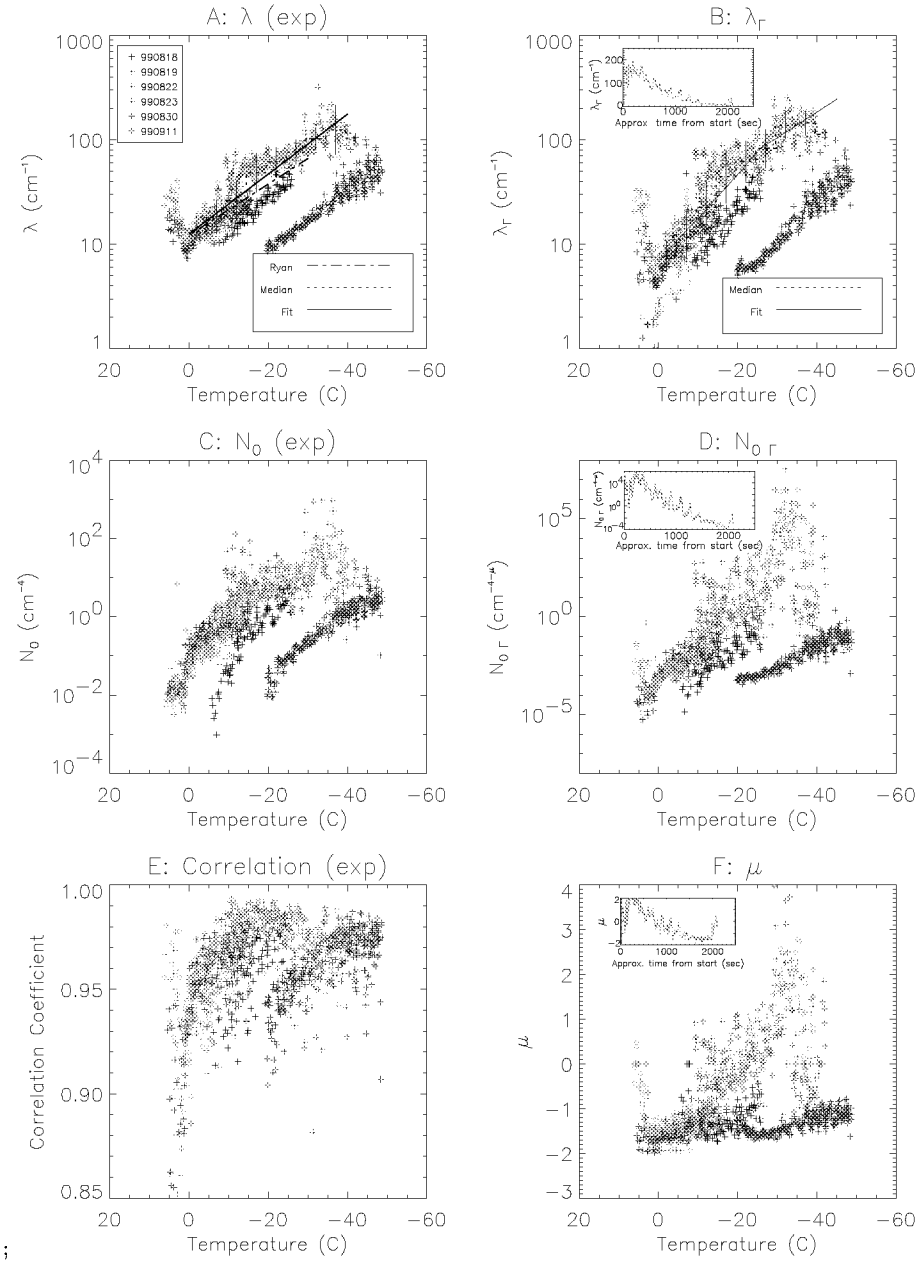

;

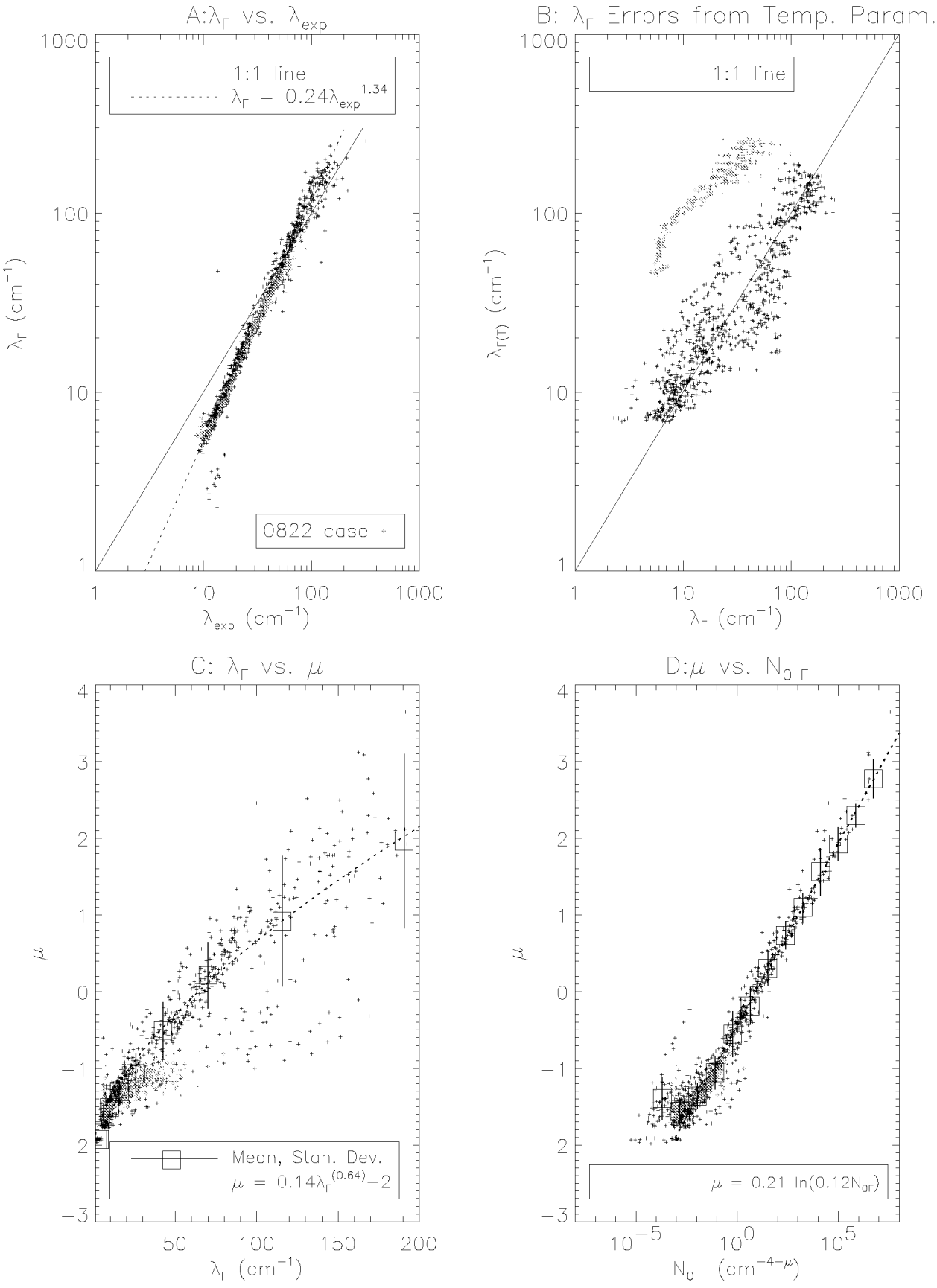
A:λΓ vs. λexp
1:1 line
λΓ = 0.24λexp^1.34
0822 case
λΓ (cm−1)
λexp (cm−1)
B: λΓ Errors from Temp. Param.
1:1 line
λΓ(T) (cm−1)
λΓ (cm−1)
C: λΓ vs. μ
Mean, Stan. Dev.
μ = 0.14λΓ^(0.64)−2
μ
λΓ (cm−1)
D:μ vs. N0 Γ
μ = 0.21 ln(0.12N0Γ)
μ
N0 Γ (cm−4−μ)

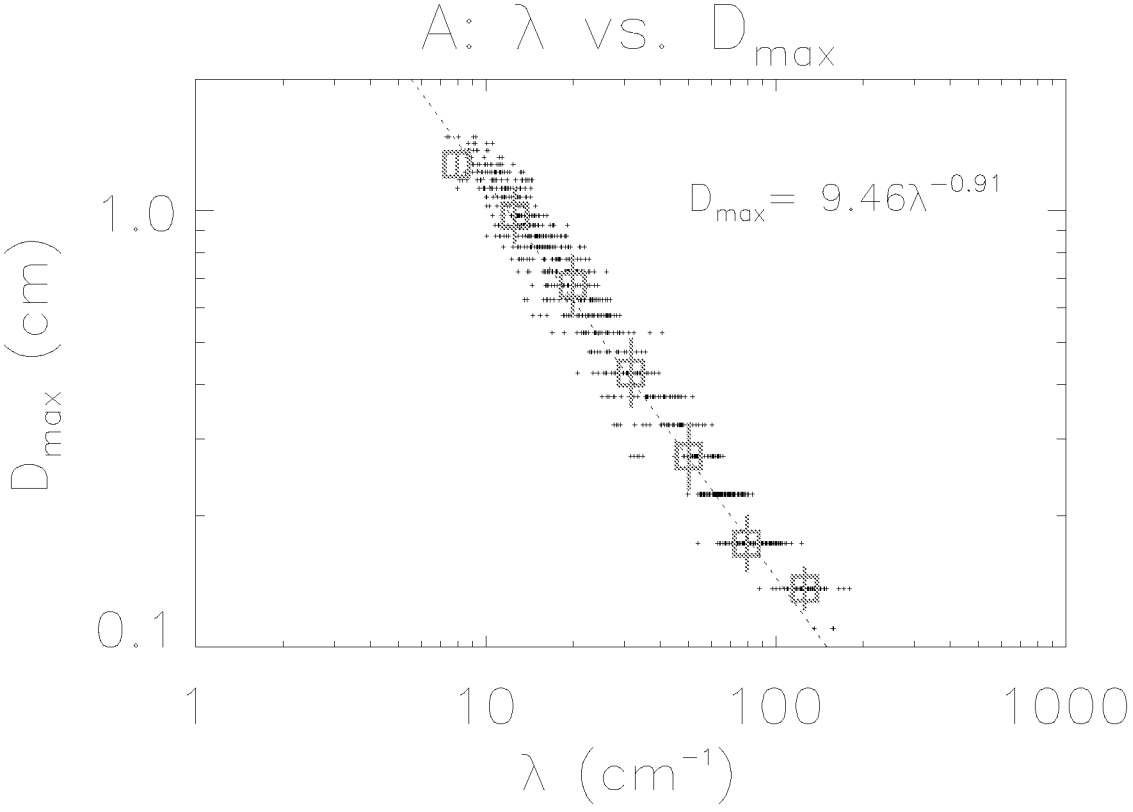
A: λ vs. D_max
D_max= 9.46λ^-0.91
1.0
0.1
D_max (cm)
1
10
100
1000
λ (cm^-1)

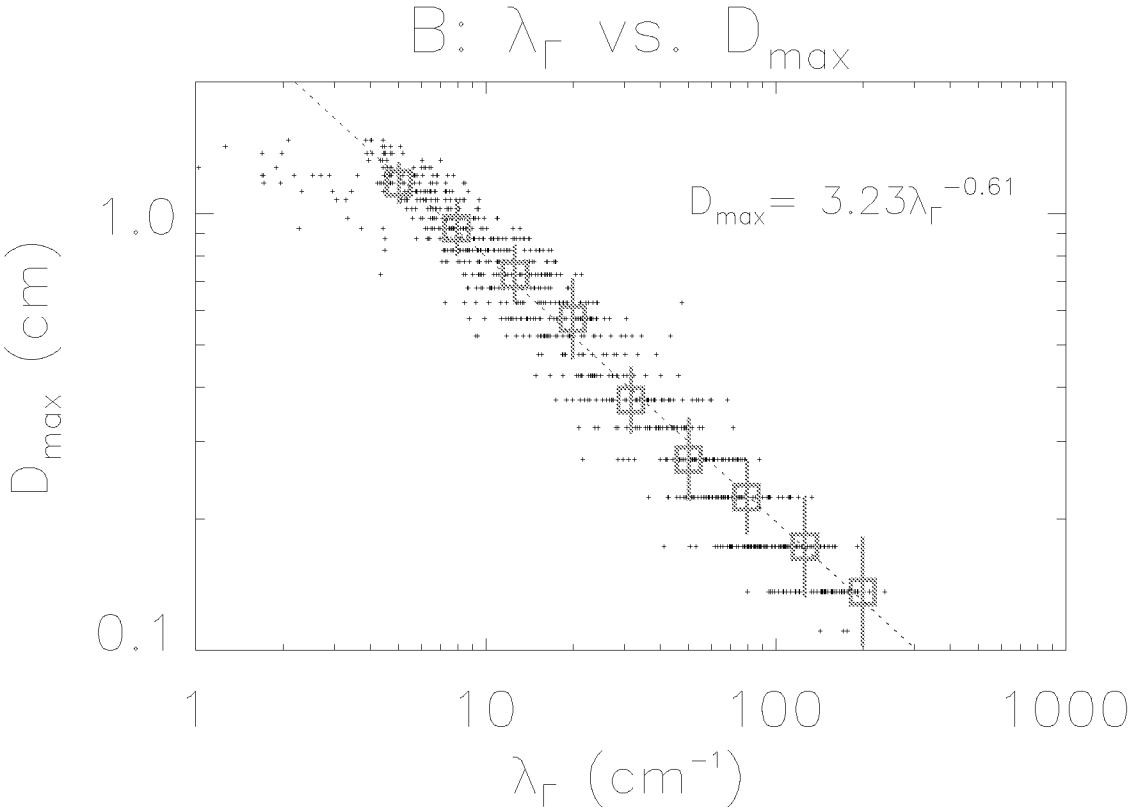
B: λ_r vs. D_max
D_max= 3.23λ_r^-0.61
1.0
0.1
D_max (cm)
1
10
100
1000
λ_r (cm^-1)

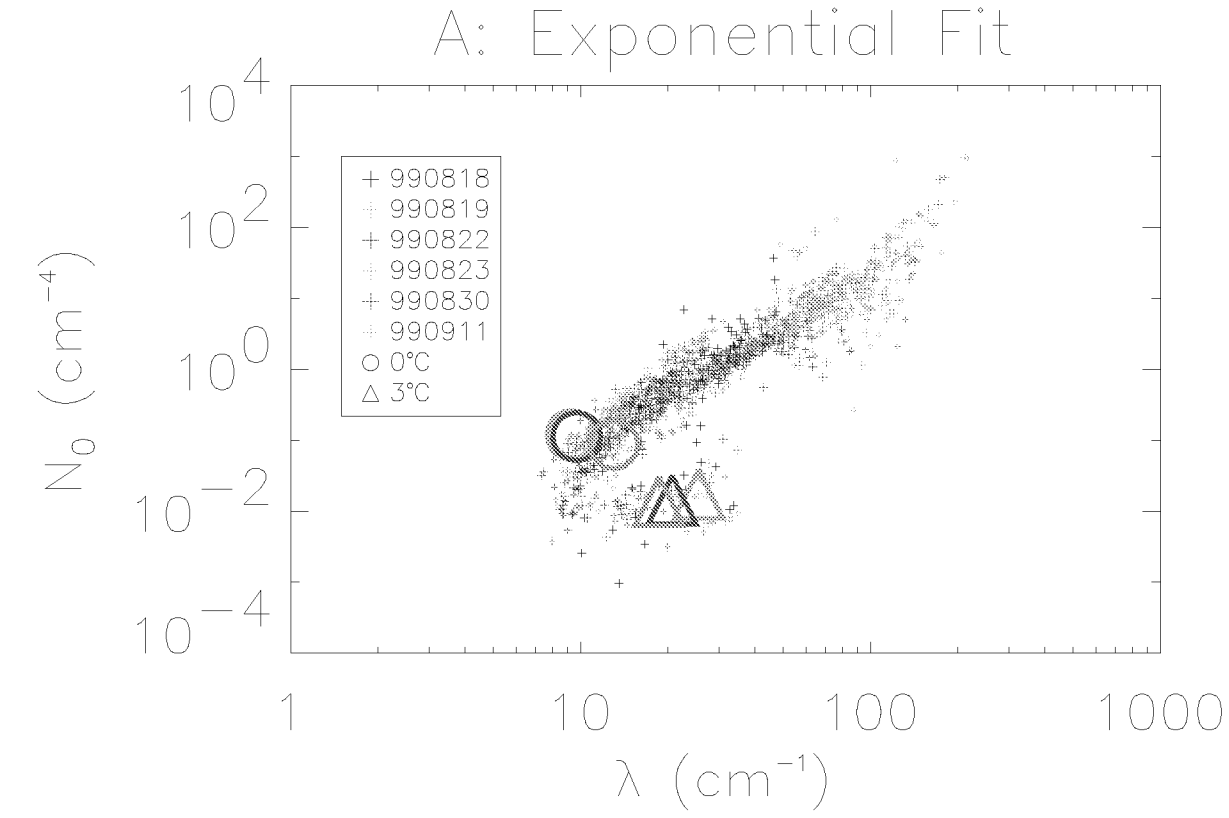
A: Exponential Fit
990818
990819
990822
990823
990830
990911
0°C
3°C
N_0 (cm^{-4})
10^4
10^2
10^0
10^{-2}
10^{-4}
1
10
100
1000
λ (cm^{-1})

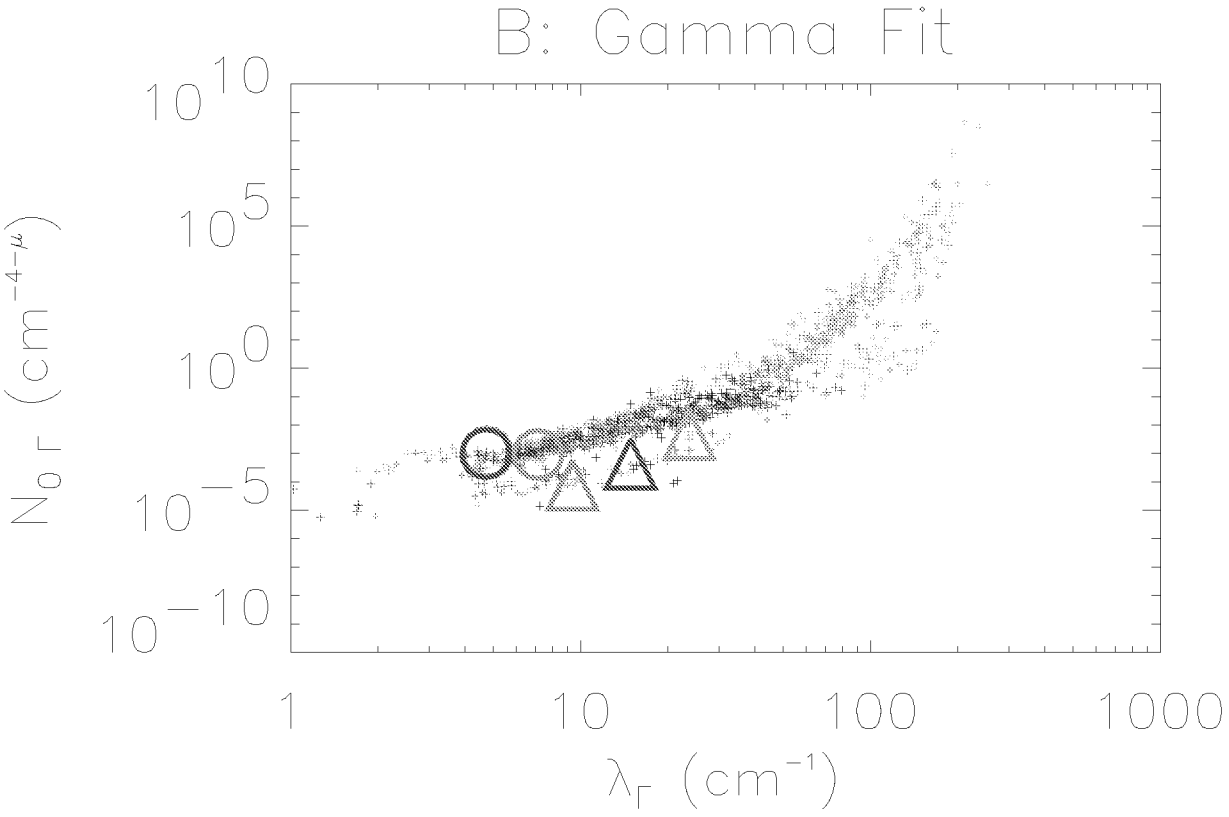
B: Gamma Fit
$N_{0\Gamma}$ (cm$^{-4-\mu}$)
10^{10}
10^5
10^0
10^{-5}
10^{-10}
1
10
100
1000
λ_Γ (cm^{-1})

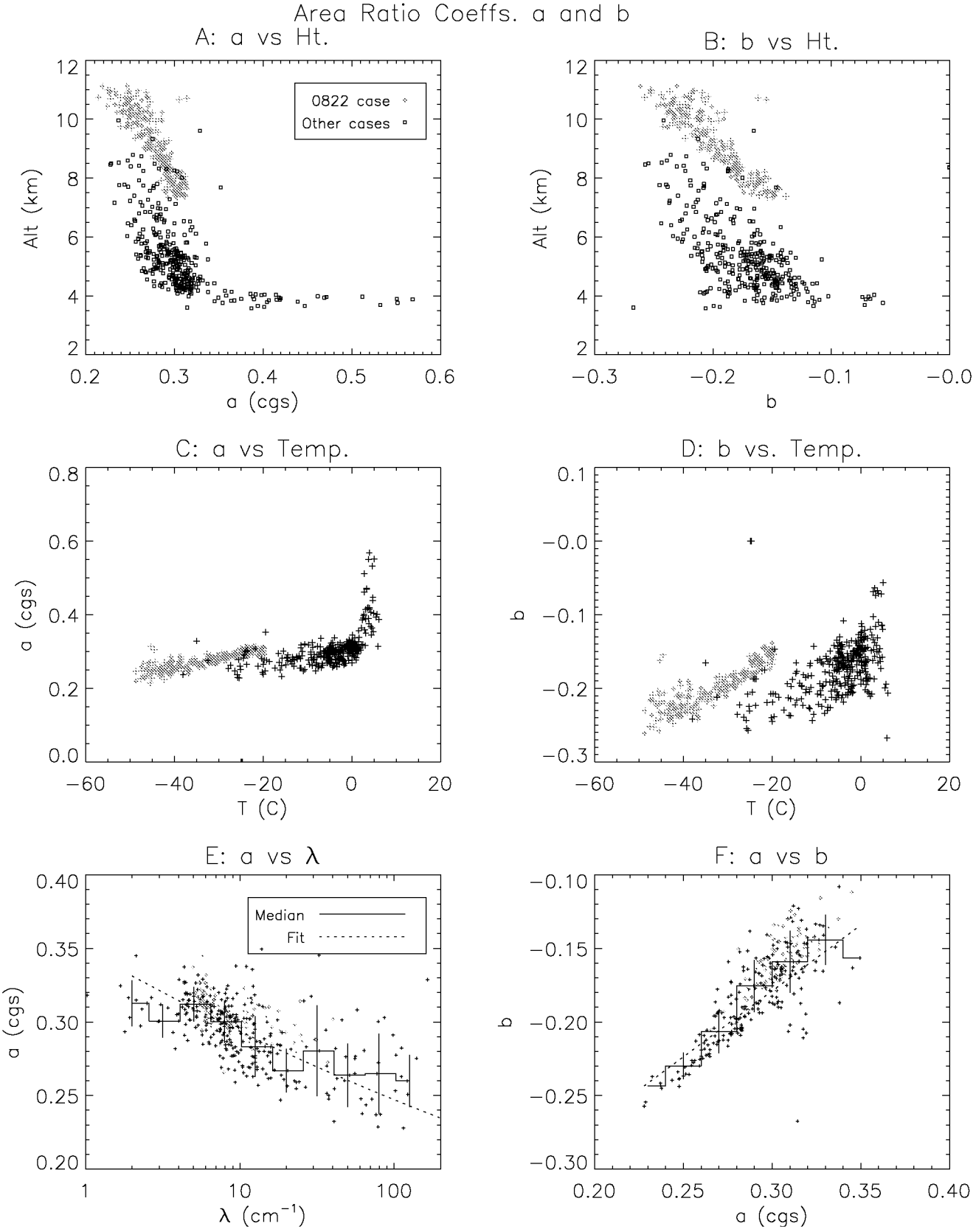
Area Ratio Coeffs. a and b
A: a vs Ht.
0822 case
Other cases
Alt (km)
a (cgs)
B: b vs Ht.
Alt (km)
b
C: a vs Temp.
a (cgs)
T (C)
D: b vs. Temp.
b
T (C)
E: a vs λ
Median
Fit
a (cgs)
λ (cm^{-1})
F: a vs b
b
a (cgs)

Fitting Errors

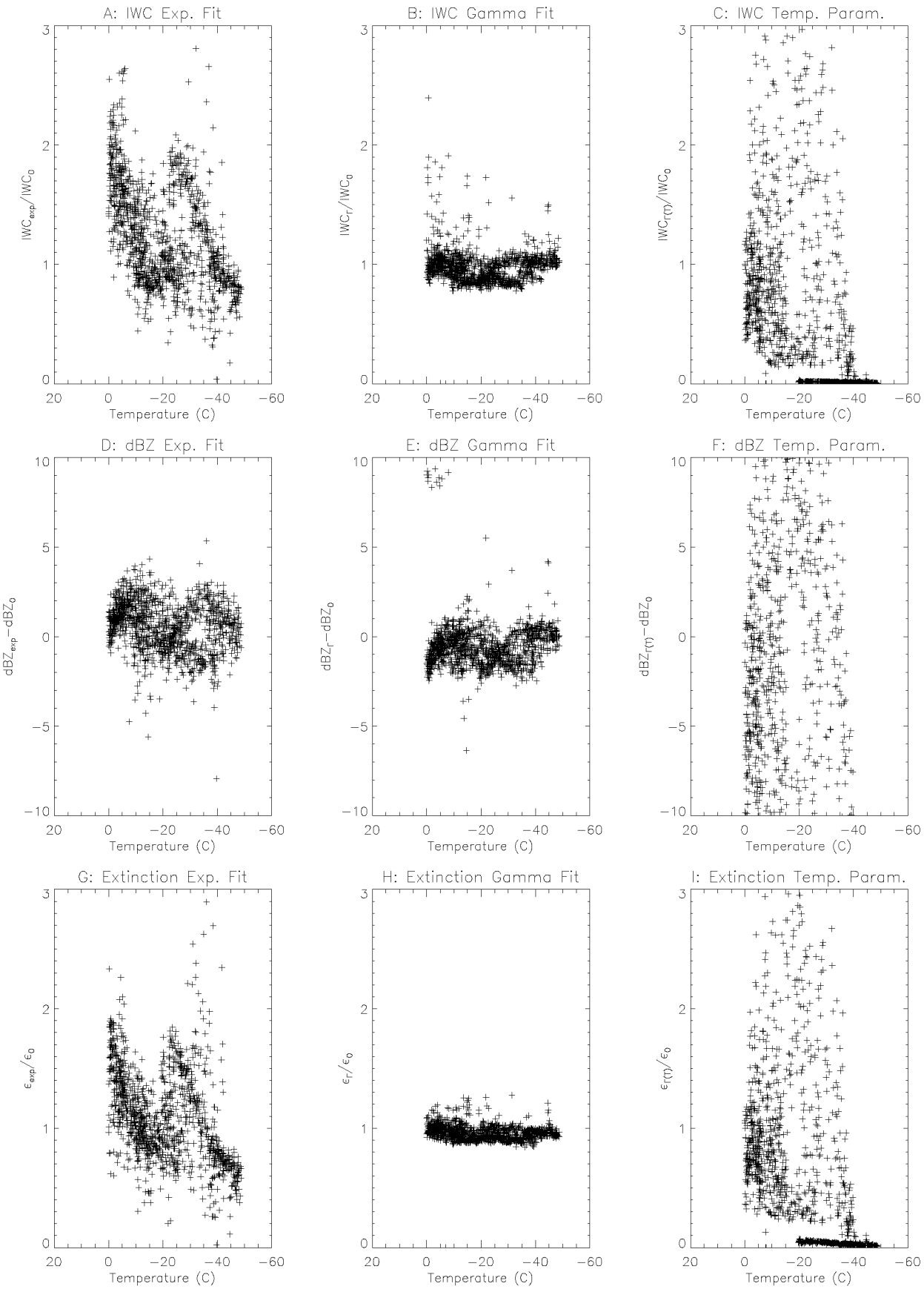

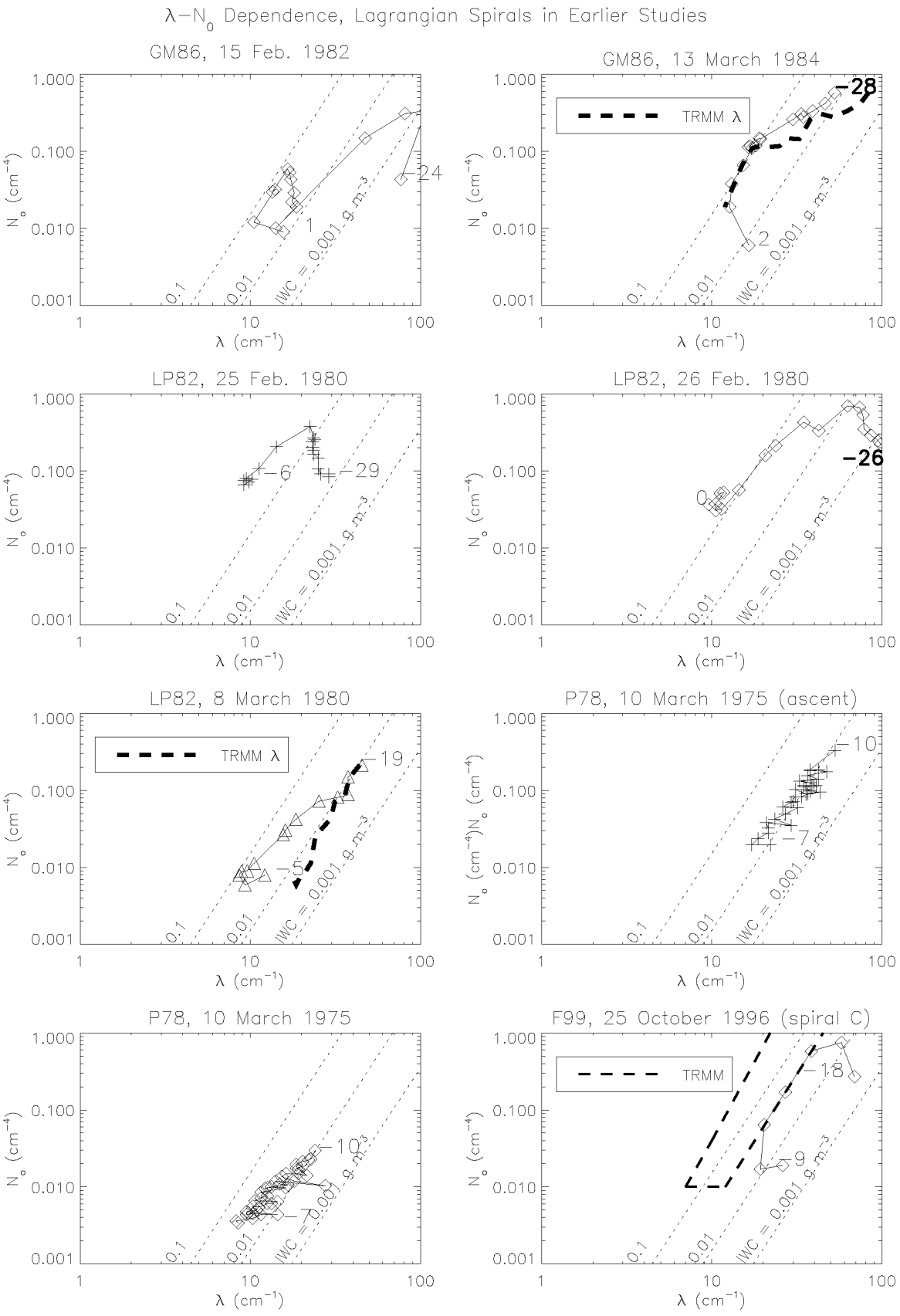
λ–N0 Dependence, Lagrangian Spirals in Earlier Studies
GM86, 15 Feb. 1982
GM86, 13 March 1984
TRMM λ
LP82, 25 Feb. 1980
LP82, 26 Feb. 1980
LP82, 8 March 1980
TRMM λ
P78, 10 March 1975 (ascent)
P78, 10 March 1975
F99, 25 October 1996 (spiral C)
TRMM
IWC = 0.001 g m-3
0.1
0.01
λ (cm-1)
N0 (cm-4)

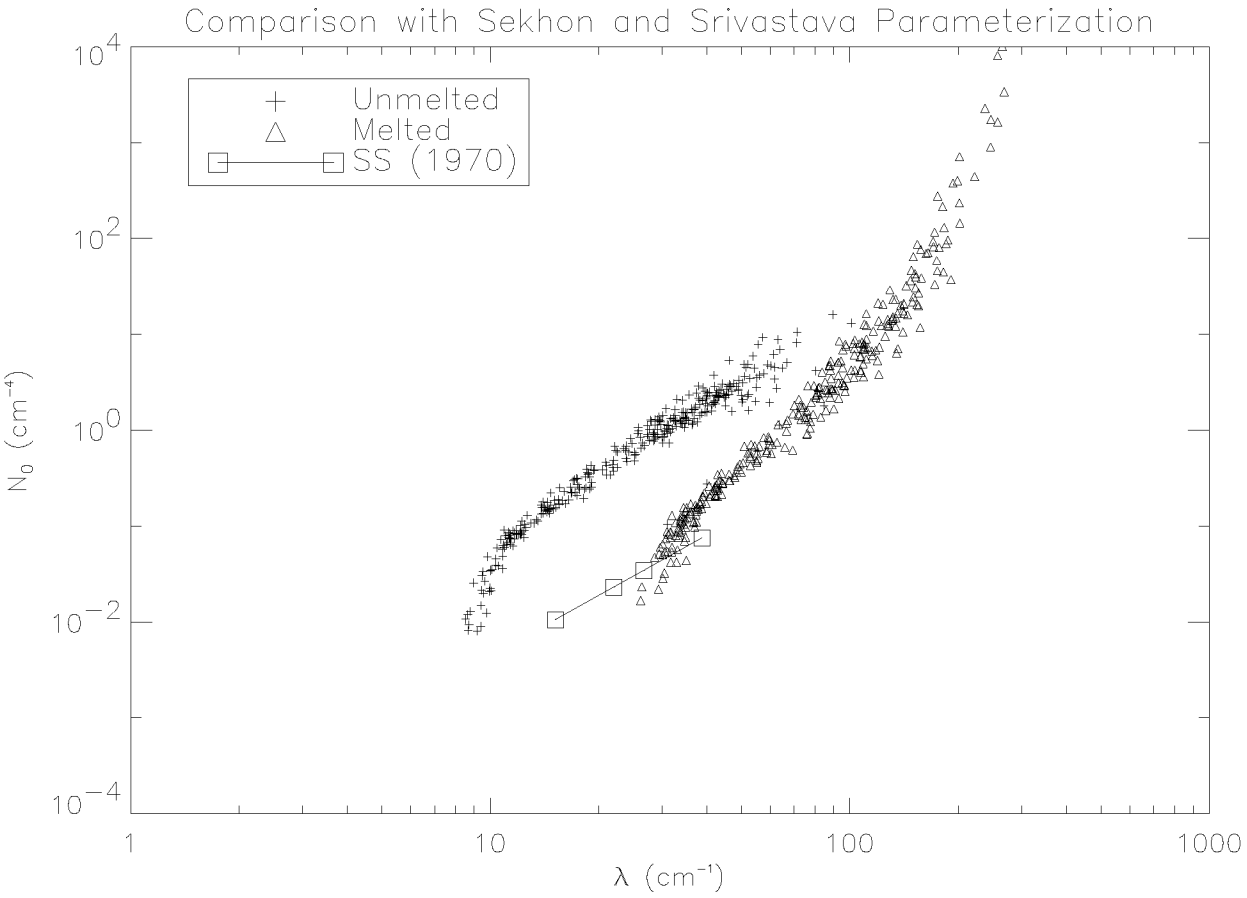
Comparison with Sekhon and Srivastava Parameterization
Unmelted
Melted
SS (1970)
10^4
10^2
10^0
10^{-2}
10^{-4}
N_0 (cm^{-4})
1
10
100
1000
λ (cm^{-1})

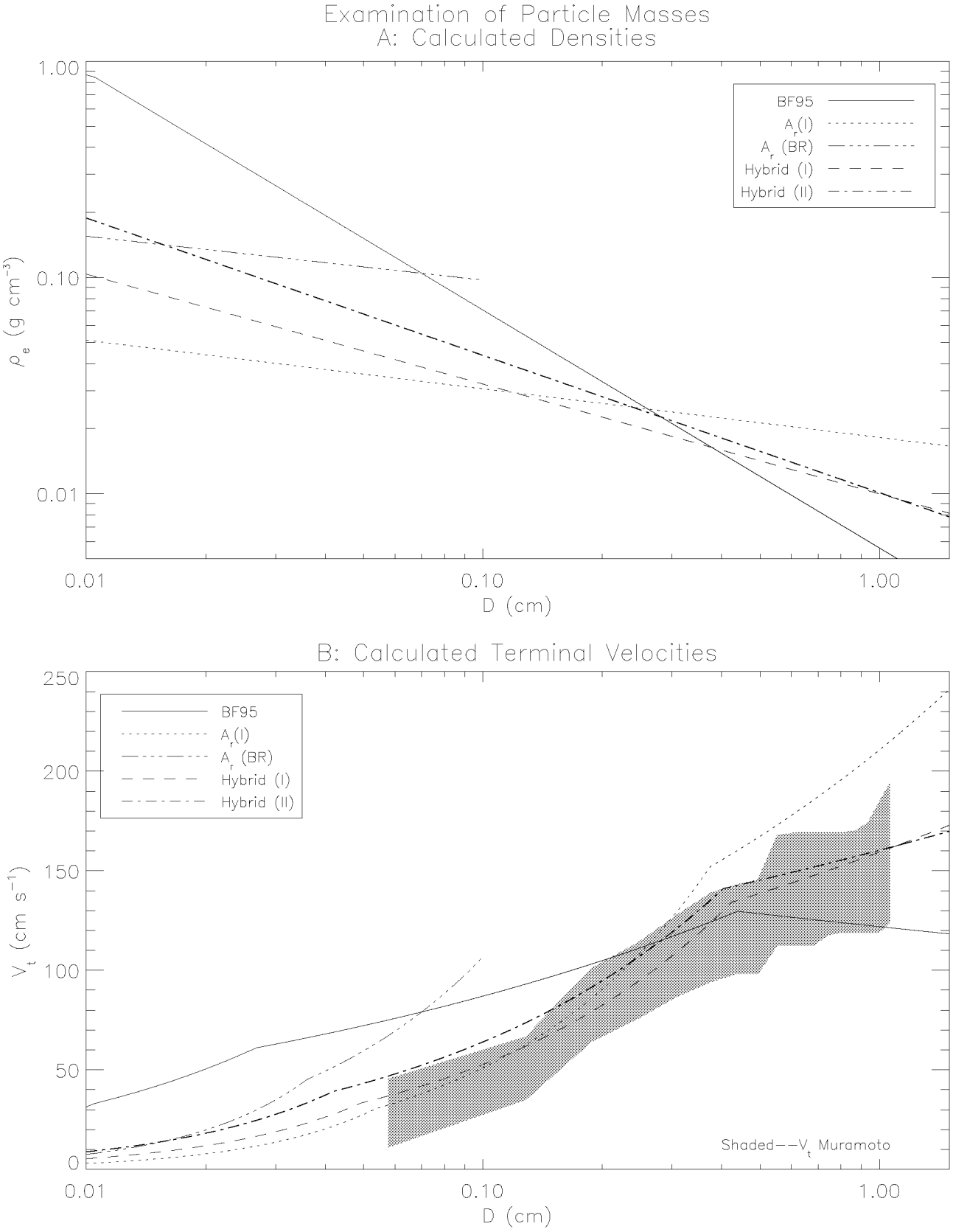
Examination of Particle Masses
A: Calculated Densities
1.00
0.10
0.01
ρ_e (g cm^{-3})
BF95
A_r(I)
A_r (BR)
Hybrid (I)
Hybrid (II)
0.01
0.10
1.00
D (cm)
B: Calculated Terminal Velocities
250
200
150
100
50
0
V_t (cm s^{-1})
BF95
A_r(I)
A_r (BR)
Hybrid (I)
Hybrid (II)
Shaded--V_t Muramoto
0.01
0.10
1.00
D (cm)

Comparison with Radar Observations